# Cloud-Resolving ICON Simulations of Secondary Ice Production in Arctic Mixed-Phase Stratocumuli Observed during M-PACE

A. POSSNER,[a] K. PFANNKUCH,[a] AND V. RAMADOSS[a]

[a] *Institute for Atmospheric and Environmental Sciences, Goethe University Frankfurt, Frankfurt, Germany*

(Manuscript received 24 April 2023, in final form 28 November 2023, accepted 7 December 2023)

ABSTRACT: Field measurements and modeling studies suggest that secondary ice production (SIP) may close the gap between observed Arctic ice nucleating particle (INP) concentrations and ice crystal number concentrations $n_i$. Here, we explore sensitivities with respect to the complexity of different INP parameterizations under the premise that $n_i$ is governed by SIP. Idealized, cloud-resolving simulations are performed for the marine cold air outbreak cloud deck sampled during the Mixed-Phase Arctic Cloud Experiment (M-PACE) with the Icosahedral Nonhydrostatic (ICON) model. The impact of the droplet shattering (DS) of raindrops and collisional breakup (BR) in addition to the existing Hallet–Mossop rime splintering mechanism were investigated. Overall, 12 different model experiments (12-h runs) were performed and analyzed. Despite the considerable amount of uncertainty remaining with regard to SIP mechanisms and their process representation in numerical models, we conclude from these experiments that (i) only simulations where DS dominates the SIP signal (potentially amplified by BR) capture observed ice-phase and liquid-phase cloud properties, and (ii) SIP events cluster around the convective outflow region and are structurally linked to mesoscale cloud organization. In addition, interactions with primary nucleation parameterizations of varied complexity were investigated. Here, our simulations show that (i) a stable long-lived mixed-phase cloud (MPC) can be maintained in the absence of primary nucleation once SIP is established, (ii) experiments using a computationally more efficient relaxation-based parameterization of primary nucleation are statistically invariant from simulations considering prognostic INP, and (iii) primary nucleation at cloud-top controls the areal extent of the mixed-phase cloud region, and reduces SIP efficacy via DS due to increased depletion of cloud liquid throughout the entire cloud column.

SIGNIFICANCE STATEMENT: Secondary ice production (SIP) remains a key challenge in our understanding of boundary layer mixed-phase clouds. Here, we use sensitivity experiments performed with the ICON model at the cloud-resolving scale to explore potential interactions between primary nucleation, SIP, and mesoscale cloud organization. We simulate an Arctic single-layer cold air outbreak stratocumulus deck that was sampled during the M-PACE campaign. We find that once established, SIP alone is sufficient to maintain the mixed-phase cloud state until the end of the simulation. Our sensitivity analysis also shows that numerically more efficient treatments of immersion freezing are statistically invariant from simulations with a full prognostic INP budget.

KEYWORDS: Arctic; Stratiform clouds; Cloud microphysics; Ice crystals; Secondary ice production; Cloud-resolving models

## 1. Introduction

Boundary layer mixed-phase clouds (MPCs) impact Earth's energy balance predominantly during boreal winter in the midlatitudes and the Arctic, and all year around in the austral midlatitudes (Korolev et al. 2017). While MPCs contain a mixture of liquid and ice, their radiative impact is governed by their liquid-phase properties in optically thick MPCs. However, these may be altered by the formation and growth of ice-phase hydrometeors through the depletion of cloud liquid by the Wegener–Bergeron–Findeisen (WBF) process (Wegener 1911; Bergeron 1935; Findeisen 1938) and riming (Ono 1969). The interactions between the ice and liquid phase in MPCs are extremely complex and remain insufficiently constrained from observations. We do know though, that the total sink on cloud condensate is strongly dependent on the ice crystal number concentration $n_i$ generated in the cloud (e.g., Vergara-Temprado et al. 2018).

These ice crystals can form via primary nucleation on available ice nucleating particles (INPs) or secondary ice production (SIP). We know that primary nucleation in boundary layer MPCs is governed by immersion freezing (Murray et al. 2012). Yet, the speciation and contributing sources of different aerosol remain poorly constrained outside targeted campaign efforts. In addition, their in-cloud processing during INP recycling remains virtually unconstrained from field observations. Contributions from SIP remain poorly constrained due to our incomplete understanding of the involved mechanisms. In general, SIP refers to the generation of an ice crystal without the presence of an INP. Seven potential SIP mechanisms have been suggested and studied in laboratory experiments

---

Denotes content that is immediately available upon publication as open access.

Supplemental information related to this paper is available at the Journals Online website: https://doi.org/10.1175/JAS-D-23-0069.s1.

*Corresponding author*: Anna Possner, apossner@iau.uni-frankfurt.de

DOI: 10.1175/JAS-D-23-0069.1

and their contributions are likely cloud regime dependent (Field et al. 2017; Korolev and Leisner 2020).

Most climate models merely consider contributions from the longest known rime-splintering mechanism by Hallet–Mossop (Hallett and Mossop 1974; Mossop and Hallett 1974). However, it is unlikely to be effective in moderately supercooled mixed-phase stratocumuli due to its limited temperature range. Fragmentation of millimeter-sized raindrops upon freezing (Lauber et al. 2018) has been shown to dominate SIP in convective clouds with relatively warm cloud bases (Sullivan et al. 2018). However, it has been shown not to contribute to SIP in Arctic stratiform clouds (Fu et al. 2019; Sotiropoulou et al. 2020). Other SIP mechanisms related to drop evaporation have also been shown to be ineffective in Arctic mixed-phase stratocumuli (Fridlind et al. 2007).

Meanwhile, field measurements indicate that droplet shattering (DS; Luke et al. 2021; Pasquier et al. 2022) or the fragmentation due to collisional breakup (BR; Rangno and Hobbs 2001; Schwarzenboeck et al. 2009) may contribute to SIP in Arctic low-level clouds. Numerical sensitivity studies of either mechanism in mixed-phase stratocumuli have shown that BR is seemingly more effective in warmer supercooled temperature ranges (Sotiropoulou et al. 2020, 2021b) and DS in colder ($T < -10°\mathrm{C}$) clouds (Sotiropoulou et al. 2020; X. Zhao et al. 2021). However, many uncertainties remain with respect to the assumptions made within these parameterizations that may alter their efficacy and thus the impact of either mechanism on cloud evolution. Furthermore, the evidence for either mechanism is largely empirical. While these process parameterizations are based on theoretical concepts, they remain to be underpinned by theoretical and experimental evidence of the actual mechanisms themselves (Korolev and Leisner 2020).

In this study, we investigate the impact of BR and DS on cloud evolution in cloud-resolving simulations, performed with the Icosahedral Nonhydrostatic Weather and Climate (ICON) model (Dipankar et al. 2015), for a case of single-layer supercooled stratocumuli observed during the Mixed-Phase Arctic Cloud Experiment [M-PACE; Verlinde et al. (2007)]. During the M-PACE campaign a single-layer, moderately supercooled, mixed-phase stratocumulus deck, which is one of the most common cloud types in the Arctic region (Morrison et al. 2012) and significantly impacts the surface energy balance (Liu et al. 2012), was sampled during three research flights complemented by ground-based remote sensing observations. This well-documented case has formed the basis of many research projects since, and was chosen for this study for the following three reasons:

First, mean cloud-top temperatures around −15°C were observed, which are well outside the Hallet–Mossop temperature range, which makes this a suitable case to study the impact of other SIP mechanisms within persistent single-layer stratocumuli. Second, first analyses, combining large-eddy simulations with in situ and remote sensing observations, showed that known mechanisms of primary ice formation and ice multiplication did not reproduce observed ice crystal number concentrations or observed lidar depolarization ratios (Fridlind et al. 2007; van Diedenhoven et al. 2009). Both studies suggest that another, yet-to-be-determined, ice formation mechanism must have been at play. Third, characterizations of INP chemical composition and spatiotemporal distribution suggest that the in-cloud budget of INP concentrations was dominated by above boundary layer, dust-containing INP concentrations (Prenni et al. 2007). This allows us to neglect the potential contributions of sea-spray INP sources for this case, which have been shown to impact marine INP concentrations in remote regions significantly (DeMott et al. 2016).

The intention of this work is threefold. First, we wish to assess the efficacy of either process in a well-established case of moderately supercooled Arctic MPCs in ICON. While ICON has been shown to adequately capture Arctic MPC fields at the cloud-resolving scale (Schemann and Ebell 2020), it has not yet been evaluated with respect to SIP in this regime. Second, we wish to explore the importance of the complexity of primary freezing parameterizations in a cloud regime where $n_i$ is seemingly dominated by SIP. Third, we wish to enhance our understanding of cloud evolution in an SIP-dominated cloud with resolved cloud-generated boundary layer dynamics.

## 2. Model and parameterizations

### a. *ICON model*

We use idealized ICON-LEM (large-eddy model) simulations in this study. The triangular grid of ICON is projected on a torus, which renders the implementation of periodic boundary conditions obsolete. The nonhydrostatic and fully compressible Navier Stokes equations are solved using C-type staggering (Zängl et al. 2015). An explicit two-time level predictor–corrector scheme is used for time integration, which treats the vertical propagation of sound waves implicitly (Dipankar et al. 2015). Furthermore, Rayleigh damping following the method of Klemp et al. (2008) is applied (Heinze et al. 2017).

The implicit treatment of sound waves, which are the fastest waves considered in the Navier Stokes equations of the atmosphere and can accelerate, or decelerate, air by altering the pressure field, requires the simulations to be run with a small time step. A basic time step $dt$ is used for tracer transport, numerical diffusion, and fast-physics parameterizations. A sub time stepping is applied for the dynamical core. Slow physics (i.e., radiation) is computed on a longer time step specified as a multiple of the basic time step (Heinze et al. 2017). Radiative fluxes are computed using ecRad (Hogan and Bozzo 2018), which was developed at the European Centre for Medium-Range Weather Forecasts (ECMWF) and implemented in ICON. Subgrid-scale turbulence is parameterized using a Smagorinsky scheme (Dipankar et al. 2015).

The cloud microphysics is parameterized with the Seifert and Beheng (2006) two-moment bulk microphysics scheme. The scheme has been used with default parameterizations summarized in Seifert and Beheng (2006), which will not be repeated here for the sake of brevity. In the following, we merely provide a summary of additional choices made regarding the physical complexity of our simulations presented in this study. For an overview of chosen setup parameters for the bulk-scheme size distributions, the reader is referred to section 3b. This bulk scheme considers two warm-phase hydrometeor species (cloud droplets and rain) and three ice-phase hydrometeors (ice, snow, and graupel).

The scheme was modified to only consider immersion freezing in these simulations. The activation of cloud droplets is calculated explicitly (Hande et al. 2016) using fits best capturing the empirical dependence of CCN concentrations on the vertical velocity at different pressure levels under European conditions without considering specific aerosol populations. Beydoun and Hoose (2019) introduced a simple scaling factor to these fits to represent CCN concentrations at different geographical locations. For the clean conditions sampled during M-PACE (CCN concentrations between 23 and 73 $\mathrm{cm}^{-3}$), we specify a scaling factor of 0.05 as suggested by Beydoun and Hoose (2019) for "very low" aerosol loading (CCN $\sim$ 30 $\mathrm{cm}^{-3}$). An additional sensitivity experiment (*PROGINP_2xCCN*; see Table 1 for a summary of all numerical experiments) with a scaling factor of 0.1 was also performed, which still yields a simulated $n_d$ consistent with the upper range of in situ $n_d$ measurements. Autoconversion, accretion, and rain self-collection are computed using the Seifert and Beheng (2006) collision–coalescence kernels.

The standard implementation of the Seifert and Beheng (2006) microphysics scheme can be executed either with prescribed INP concentrations for immersion freezing, or using a simplified, spatiotemporally varying implementation of INP. The latter implementation requires the simulation to be run with two additional tracers, which are advected with the flow. One tracer stores the background concentration of INP, and the other the activated fraction $\mathrm{in}_{\mathrm{act}}$. Here, we initialize the INP concentrations using the temperature dependence of INP following the DeMott et al. (2015) parameterization. In regions subsaturated with respect to ice, the activated fraction is relaxed back to zero over a characteristic prescribed time scale $\tau_{\mathrm{relax}}$:

$$\mathrm{in}_{\mathrm{act}} = \mathrm{in}_{\mathrm{act}}\left(1 - \frac{dt}{\tau_{\mathrm{relax}}}\right). \tag{1}$$

In cases with significant surface precipitation (frozen), the background INP concentration will be depleted in the absence of an INP source. During M-PACE, surface precipitation rates remained below 1 mm per day (Klein et al. 2009).

There is no significant increase in computation time associated with the addition of these two tracers, whereas the implementation of the prognostic primary nucleation with active SIP conditions increases the simulation time threefold. Once activated, the cloud droplets grow through vapor diffusion and collisional growth processes, including riming. Once nucleated, the ice crystals grow through deposition and collisional growth processes, including riming. In its operational form, the Seifert and Beheng (2006) parameterization merely considers the Hallet–Mossop rime splintering process.

TABLE 1. Summary of sensitivity experiments. Experiments differ by the specified INP treatment, the inclusion of DS and/or BR, and RF assumptions made within the BR scheme.

| Simulation | INP | DS | BR | RF |
|---|---|---|---|---|
| *PROGINP_ctl* | Prognostic | Off | Off | — |
| *PROGINP_RF02* | | Off | On | 0.2 |
| *PROGINP_RF03* | | Off | On | 0.3 |
| *PROGINP_RF04* | | Off | On | 0.4 |
| *PROGINP_DS* | | On | Off | — |
| *PROGINP_RF01_DS* | | On | On | 0.1 |
| *PROGINP_RF02_DS* | | On | On | 0.2 |
| *PROGINP_noPRIM* | No immersion freezing after 4 h | On | On | 0.1 |
| *PROGINP_10INP* | Prognostic with 10 × INP | Off | Off | — |
| *PROGINP_2xCCN* | Double CCN concentration | On | On | 0.1 |
| *RELINP_DS* | | On | Off | — |
| *RELINP_RF01_DS* | | On | On | 0.1 |
| *RELINP_RF02_DS* | | On | On | 0.2 |

### b. *Prognostic representation of primary nucleation*

In addition to the characteristic time-scale formulation associated with INP cycling, we assess the impact of SIP in simulations with a full prognostic treatment of INP with reduced complexity. This formulation follows the approach suggested by Solomon et al. (2015), which uses the following budget equation for INP concentrations:

$$\frac{\partial \mathrm{INP}}{\partial dt} = \mathrm{ADV} + \mathrm{DIFF} + \left.\frac{\partial \mathrm{INP}}{\partial dt}\right|_{\mathrm{nuc}} + \left.\frac{\partial \mathrm{INP}}{\partial dt}\right|_{\mathrm{subl.}}, \tag{2}$$

where ADV and DIFF refer to the rates of change in INP due to advection and turbulent diffusion. The nucleation term represents the loss of INP through nucleation (in this case immersion freezing) and the sublimation term refers to the INP replenished by fully sublimating ice crystals. Using this approach, Solomon et al. (2015) demonstrated the importance of INP recycling for the maintenance of Arctic MPCs governed by primary nucleation.

The INP concentrations are initialized following the empirical fit of DeMott et al. (2015):

$$\mathrm{INP}(T) = cN_a^{[\alpha(273.16-T)+\beta]}e^{[\gamma(273.16-T)+\delta]}. \tag{3}$$

Here, $N_a$ describes the number of aerosol particles with diameters larger than 0.5 $\mu\mathrm{m}\ \mathrm{cm}^{-3}$ and $T$ denotes the temperature in kelvins. The other constant parameters have the following values: $c = 10^3$, $\alpha = 0.0$, $\beta = 1.25$, $\gamma = 0.46$, and $\delta = -11.6$. This curve is divided into 15 temperature bins. Each bin holds the amount of potential INP within a certain temperature range at each location and each point in time. Thus, this scheme adds 15 tracers to the computation. If the environmental temperature falls below the lower temperature bound, of a given INP bin in a saturated (with respect to water) grid box at a given time step, 50% of the INP concentration within this temperature bin and grid box are nucleated and removed instantaneously (Solomon et al. 2015). The initialization of this scheme for M-PACE is specified in section 3b.

The INP will be removed from each bin during immersion freezing events when lwc > $10^{-3}$ g $\mathrm{kg}^{-1}$ and the atmospheric temperature is at, or below, the temperature of each of the 15 bins considered. When frozen hydrometeors with immersed INP sublimate, these INP are once again released and may freeze again if re-entrained into the liquid cloud layer. During our M-PACE simulations, the atmosphere is subsaturated with respect to ice below 714 m. The implemented INP source through sublimation is proportional to the amount of depletion within each bin via immersion freezing. This is achieved using weighting functions:

$$w_{k,t} = \frac{\widetilde{\text{INP}}(k,\,0) - \widetilde{\text{INP}}(k,\,t)}{\widetilde{\text{INP}}(k,\,0)}, \tag{4}$$

for each temperature bin $k$ at time $t$. The weights $w_{k,t}$ are normalized such that $\sum_{k=1}^{15} w_{k,t} = 1 \forall t$. The term $\widetilde{\text{INP}(k,\,t)}$ describes the accumulated total number of INP in temperature bin $k$ of the entire simulation domain at time $t$. Upon sublimation, INP in each temperature bin $k$ is replenished in proportion to $w_{k,t}$, and the temporally varying bulk INP number concentration contained at each grid point in all frozen hydrometeor species. For this accounting three INP tracers (for ice, snow, and graupel) were implemented in addition to the 15 temperature-bin INP tracers.

Thus, the source (sublimation) and sink (nucleation) terms of INP in this prognostic INP scheme are diagnostic. This simplification of INP nucleation is justified by the considerably stronger dependence of the immersion freezing rate calculated by classical nucleation theory on temperature than differences in time step (Ervens and Feingold 2013). The implications of the simplifications made in this prognostic scheme of reduced physical complexity are further discussed in section 6 and summarized in the conclusions.

When SIP is active, $n_i$ may be dominated by SIP. We thus need to track primary and secondary ice, snow, and graupel hydrometeors to prevent the artificial generation of INP through sublimating secondary hydrometeors. This is further described in more detail in section 2e. Overall, the computational cost is approximately tripled when a prognostic INP budget is considered in the presence of SIP.

### *c. Implementation of droplet shattering*

The Phillips et al. (2018) parameterization for DS is implemented in ICON. The empirical scheme considers two types of collisions: (i) collisions between raindrops and smaller ice crystals or snowflakes and (ii) collisions between raindrops and larger snowflakes or graupel. For the first type of collisions, an empirical formula is fitted against laboratory data in the temperature range from −4° to −25°C and for raindrop sizes between 0.06 and 1.6 mm. Furthermore, either "big" fragments or "tiny" splinters may be generated by the shattering raindrop. This is included in the parameterization in terms of two separate functional fits for the total number of generated fragments $n_t$ and the number of ejected large fragments $n_b$ per collision. Further details on the functional form, accuracy of the fit and used laboratory observations are provided in Phillips et al. (2018). The basic structure of the empirical formula describing $n_{t,1}$ and $n_b$ is repeated here:

$$n_{t,1} = \Xi(D)\Omega(D)\left[\frac{\zeta\eta^2}{(T - T_0)^2 + \eta^2} + \beta T\right] \quad \forall m > m_f \quad \text{and} \tag{5}$$

$$n_b = \min\left\{\Xi(D)\Omega(D)\left[\frac{\zeta_b\eta_b^2}{(T - T_{b,0})^2 + \eta_b^2}\right],\, n_{t,1}\right\}, \tag{6}$$

where $T$ denotes the temperature (°C); $D$ and $m$ are the diameter and mass of the raindrop respectively; and $m_f$ is the mass of the colliding frozen ice or snow crystal. The terms $\Xi$ and $\Omega$ denote threshold functions for the onset of fragmentation through DS in terms of size and temperature, and $\eta$, $\eta_b$, $\zeta$, $\zeta_b$, $T_0$, and $T_{b,0}$ are derived by the fit. The mass of the fragments is calculated assuming $m_{t,1} = \rho_i \pi D_t^3/6$ with $\rho_i = 920$ kg m$^{-3}$ and $D_{t,1} = 10\ \mu$m. Big splinters are added to the graupel category and small splinters to the ice category.

For collisions of the second kind, the formulation for the number of ejected particles per collision $n_{t,2}$ is proportional to the ratio $r_e$ of the available kinetic energy of the collision $e_k$ to the surface energy:

$$n_{t,2} = 3\Phi(T) \times [1 - f(T)] \times \max\{r_e - r_{e,c},\, 0\}$$
$$\forall m > m_f \quad \text{and} \quad D > 150\ \mu\text{m}, \tag{7}$$

where $f(T)$ denotes the frozen fraction and $\Phi(T)$ is a function of the frozen fraction and the required minimum energy ratio $r_{e,c}$ is prescribed as 0.2. All ejected crystals are assumed to be of the same mass, which is specified as $m_{t,2} = 0.001m$.

### *d. Implementation of collisional breakup*

A parameterization based on energy conservation during collisions proposed by Phillips et al. (2017) is implemented. This parameterization computes the number of ejected particles per ice–ice collision $n_{\text{br}}$ as a function of $e_k$, the surface area of the smaller colliding particle $\alpha$ multiplied by the asperity surface density $A$:

$$n_{\text{br}} = \alpha A\left\{1 - \exp\left[-\left(\frac{Ce_k}{\alpha A}\right)^{\gamma}\right]\right\}. \tag{8}$$

The argument of the exponential function denotes the ratio between $e_k$ and the work required to break off asperities in the region of contact. The term $C$ denotes the asperity-fragility coefficient, which is prescribed as 10 815 for dendrites and as 24 780 for spatial planar crystals. The final parameter $\gamma$ is related to the degree of riming as $\gamma = 0.5 - 0.25\text{RF}$, where RF denotes the rimed fraction (rimed mass contribution to the total mass of frozen hydrometeor). Recent observations demonstrate that substantial amounts of in-cloud riming are indeed found in marine mixed-phase stratocumuli (Lasher-Trapp et al. 2021; Tornow et al. 2021; Waitz et al. 2022). However, the rimed fraction was not quantified. Meanwhile, mean rimed fractions as high as 0.3 have been diagnosed in mixed-phase clouds (Maherndl et al. 2023) sampled during the High Altitude and Long Range Research Aircraft HALO-(AC)$^3$ campaign.

Note that $A$ is primarily determined by the crystal habit, size, and RF of the smaller colliding particle. It is thus indirectly a function of $T$ and supersaturation with respect to ice, which determines the habit and growth history of the shattering ice crystal. The scheme considers ice–ice, ice–snow, snow–snow, ice–graupel, snow–graupel, and graupel–graupel collisions. Different expressions for $A$ and $C$ are used depending on the hydrometeor type of the smaller colliding particle [see Table 1 of Phillips et al. (2017)]. All generated fragments are initialized with 0.1% of the mass of the colliding particles, and are transferred to the ice category.

### e. *Treatment of primary and secondary ice*

The implementation of a prognostic INP budget (section 2b) under active SIP conditions requires a separate tracing of primary and secondary ice to prevent artificial INP generation. Figure 2 in X. Zhao et al. (2021) shows that in the simulated temperature range during M-PACE up to 100 fragments per collision may be generated. Not tracing INP, and thus primary ice until sublimation, may artificially increase background INP concentrations by several orders of magnitude over time.

To overcome this issue, six new additional tracers are implemented for the mass and number concentration of secondary ice, snow, and graupel (virtually nonexistent in our simulations, but implemented for completeness) in addition to the 10 tracers carrying the information of mass and number concentration of the five hydrometeor species (cloud, rain, ice, snow, and graupel). Hydrometeors described by these modes do not contain INP but otherwise undergo the exact same processes as primary ice, snow, and graupel.

The purpose of these new tracers is to distinguish crystals containing (at least one) INP, or none. Thus, following aggregation between colliding primary and secondary frozen hydrometeors, the resulting aggregate is shifted into the primary category. The resulting splinters from BR through primary ice with primary ice collisions, are shifted into the secondary ice category and removed from the primary ice budget. This accounting is also performed for DS, if the shattering is triggered by collisions through primary frozen hydrometeors and raindrops.

## 3. Observations and simulation setup

### a. *M-PACE case and observations*

Our case study focuses on the single-layer cloud deck sampled during M-PACE between 9 and 10 October 2004 (Verlinde et al. 2007) along the North Slope of Alaska. During this time a strong capping inversion (Fig. 1a) formed under a persistent high pressure system (subsidence of $-8.2 \times 10^{-3}$ m s$^{-1}$ at cloud top). Meanwhile, cloud formation was governed by strong sensible and latent surface heat fluxes during a cold-air outbreak event, where boundary layer air was advected with $-13$ m s$^{-1}$ in the zonal direction and $-3$ m s$^{-1}$ in the meridional direction from the Arctic ice shield to the open ocean surface.

The soundings shown in Figs. 1a and 1b are available from the Atmospheric Radiation Measurement (ARM) station at Utqiaġvik. Profiles of liquid water content (lwc; Fig. 1c) and ice water content (iwc; Fig. 1d) are obtained from the "Continuous Baseline Microphysical" (MICROBASE) retrieval product (Wang 2007). The retrieval uncertainty documented for each variable is 18% and up to 100% respectively. These value-added baseline retrievals of cloud properties are obtained from a combination of the 35-GHz millimeter-wavelength cloud radar, micropulse lidar, and microwave radiometer (Giangrande and Jensen 2002). Peak values of iwc reach around 6% of the observed peak in lwc. Estimates of vertically integrated quantities (Shupe et al. 2006; Turner et al. 2007), namely liquid (lwp) and total ice (tiwp) water paths, were also based on the combined lidar/radar retrievals at Utqiaġvik and Oliktok Point and are provided as lwp = 160 ± 50 gm$^{-2}$ and tiwp = 15 ± a factor of 2 (i.e., the ice water path could be between 8 and 30 gm$^{-2}$).

The uncertainties reflect the retrieval uncertainties provided by the authors. However, the true uncertainty in tiwp is likely considerably higher than a factor of 2 (Zhao et al. 2012), which in particular impacts the lower bound of the tiwp retrieval. The uncertainties in ice and water mass retrievals of multiple ground-based remote sensing products in Arctic overcast boundary layer clouds were investigated in Zhao et al. (2012). Similar to previous work (e.g., Heymsfield et al. 2008), it was shown that differences in cloud mask and phase diagnostics across different products, as well as crystal habit and particle size distribution assumptions, considerably impact the relationship between radar reflectivity and retrieved iwc and tiwp. Thus, the true uncertainty in the tiwp retrieval may reach up to 100%.

In situ measurements of $n_d$ and $n_i$ from three staircase research flights performed between Utqiaġvik and Oliktok Point are available. McFarquhar et al. (2007) inferred $n_d$ from the forward scattering spectrometer probe (FSSP), which measures particle diameters between 3 and 53 $\mu$m, providing 10-s running averages. Meanwhile, $n_i$ is inferred from a combination of different cloud probes measuring at different size ranges. This includes the one- and two-dimensional cloud probes, which measure in size ranges between 20 and 620 $\mu$m, and 30 and 960 $\mu$m, and the high-volume precipitation sampler, which measures particles between 0.4 and 40 mm. Within the mixed-phase regime, which is identified using the Rosemount Icing Detector, all particles larger than 125 $\mu$m are identified as ice particles. Particles with diameters between 53 and 125 $\mu$m are identified as ice in the absence of drizzle. All spherical particles in this size range were identified as drizzle. However, merely 19% of all cloud images obtained from the cloud particle imager contained at least one spherical hydrometeor (McFarquhar et al. 2007). Thus, the bulk of all measurements indeed contained ice crystals in this size range.

The $n_i$ measurements obtained during M-PACE are still susceptible to artificial shattering at the inlet of the cloud probes, which is mitigated by antishattering coatings on tips used in later field campaigns. Several studies estimate that this can artificially increase measured $n_i$ by a factor of 2–5 (e.g., Field et al. 2003; Febvre et al. 2012), and in some data samples up to a factor of 10 (Korolev et al. 2011), though many of these fragments are likely to be smaller than the required minimum diameter of 53 $\mu$m (Febvre et al. 2012) for the $n_i$ estimate. Nonetheless, all ice crystal measurements with diameters less than 500 $\mu$m are prone to biases by inlet shattering. Thus, a correction factor of 0.25 is applied to $n_i$

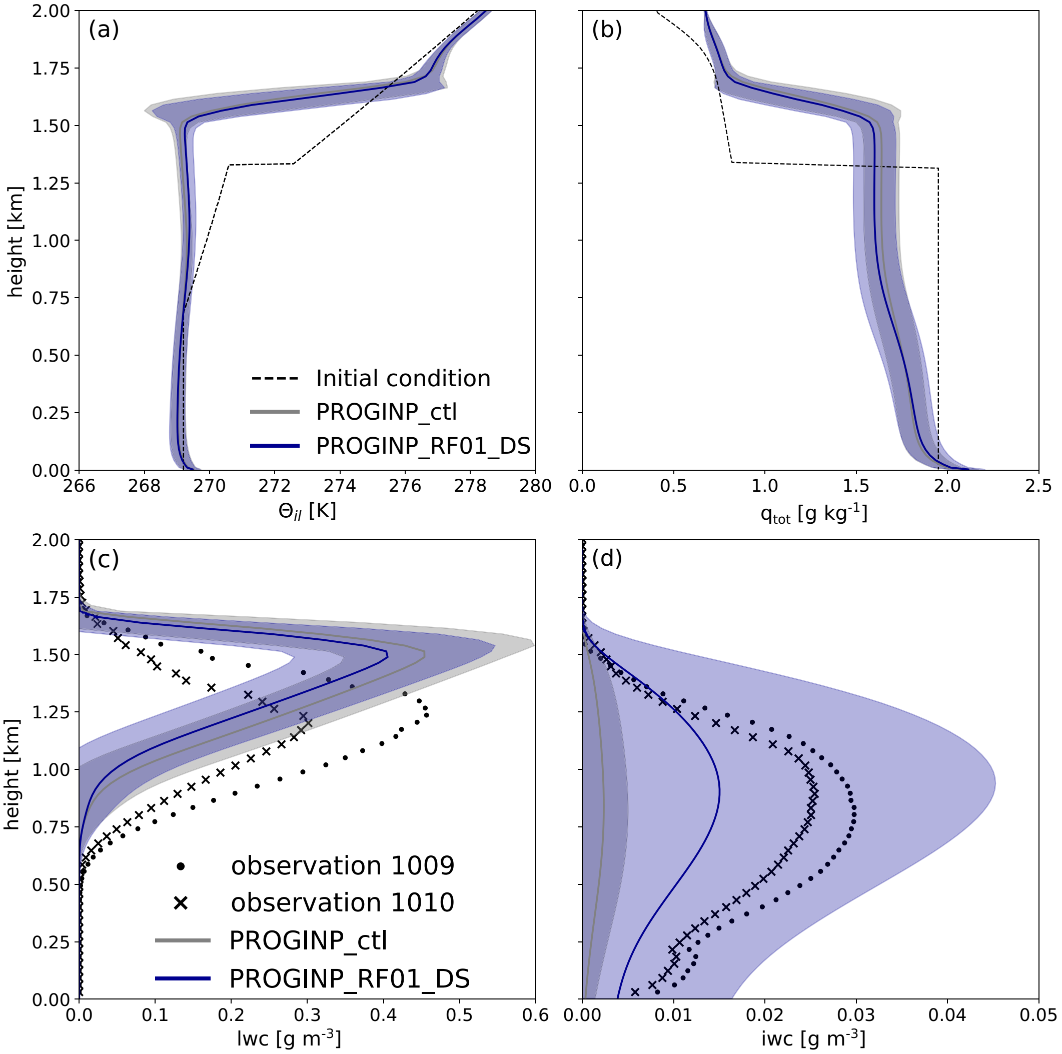

FIG. 1. Soundings of (a) ice–liquid potential temperature $\theta_{il}$ and (b) total water content $q_{tot}$ (including ice crystal mass contribution) obtained from the 1700 UTC 9 Oct 2004 sounding at Utqiaġvik, in comparison with simulated thermodynamic profiles for two sensitivity experiments defined in Table 1. The soundings were smoothed in the vertical direction to improve the model performance as in Klein et al. (2009). Also shown are remote sensing estimates for (c) liquid water content (lwc), and (d) total ice water content (iwc), giving spatiotemporal averages (solid lines) and standard deviations (color shading) following model spinup. Information on measurement uncertainty of the cloud retrievals is provided in the main text. The labels “1009” and “1010” refer to the two different research flights flown on 9 and 10 Oct 2004, respectively.

measurements from McFarquhar et al. (2007), as suggested by Jackson and McFarquhar (2014) and Jackson et al. (2014).

### b. *Simulation setup*

The cloud-resolving simulations are performed on a 25 × 22 km$^2$ domain with an edge length (length of one side of an equilateral triangle) of 125 m. The simulations are run for a 12-h period with a time step of 1 s. The slow time step (for the radiation scheme) is set to 10 min. All simulations are performed with 144 vertical levels and a domain top of 23 km. In the lowest 2.1 km of the atmosphere a vertical resolution of 25 m is prescribed. Above this threshold, the vertical resolution decreases with height. Rayleigh damping is applied from an altitude of 3 km upward.

The simulations are initialized with the 1700 UTC sounding obtained at Utqiaġvik on 9 October 2004. The large-scale forcing for subsidence and the horizontal advection of moisture and heat are based on ECMWF analysis fields and is prescribed as in Klein et al. (2009). The simulations are performed with a fixed sea surface temperature (SST) of 272 K and interactive surface fluxes. The prescribed SST is lower than in the Klein et al. (2009) experiments, where an SST of 274 K was prescribed. However, it is within the range of the ERA5 reanalysis and representative of near-ice edge conditions at Utqiaġvik. Meanwhile, the SST prescribed in Klein et al. (2009) is representative of conditions farther downwind. The SST adjustment was necessary in our simulations. A prescribed SST of 274 K induced excessive boundary layer deepening during the first 10 h of simulation time (not shown), which resulted in a 500-m bias in boundary layer depth. Simulations with reduced SST resulted in lower interactive surface fluxes, and a more stable boundary layer top. The surface fluxes themselves remain unconstrained from observations, and are on average 60% lower than the sensible heat flux of 136 W $m^{-2}$ and 19% lower than the latent heat flux of 108 W $m^{-2}$ obtained from ERA-5.

Two different types of experiments are performed using either a prognostic budget implementation for INP (section 2b), or a computationally more efficient approach characterized by $\tau_{\mathrm{relax}}$ (section 2a). These will be referred to as *PROGINP* and *RELINP* experiments from here on. During M-PACE, a mean INP concentration of 0.16 $l^{-1}$ was measured (Prenni et al. 2007). We thus specify $N_a$ in Eq. (3) as 7.5 $cm^{-3}$, such that on average the sum across all temperature bins available for nucleation, at a given cloud-top temperature, equals the observed INP concentration.

The warmest temperature bin contains all available INP down to a temperature of −7.7°C, which corresponds to the warmest cloud base temperature of the simulation. A bin width of 0.75°C was specified to cover the entire possible temperature range within the simulated cloud layer given an average cloud-top temperature of −17.5°C. To provide comparable INP conditions, the immersion freezing of the *RELINP* was adjusted such that the background INP are also calculated consistent with Eq. (3) using similar parameter specifications as in *PROGINP*.

The default BR parameterization considers a temperature-dependent habit classification of dendrites between −12° and −17°C and spatial planar between −9° and −12°C and between −17° and −40°C (Phillips et al. 2018). As this formulation introduces an instantaneous habit change throughout the simulated cloud profile during M-PACE, we run the simulations with a fixed habit categorization of spatial planar in the BR parameterization, which qualitatively is consistent with cloud particle imager images, although large amounts of spherical ice were also observed in the upper half of the cloud (McFarquhar et al. 2007). The habit characteristics of all hydrometeors for this simulation are summarized in Table 2. The size distribution of cloud droplets is described by a classical Γ-distribution, while exponential distributions are used for rain, ice, and snow. The graupel size distribution is parameterized with a generalized Γ-distribution.

The *PROGINP* experiments contain six new hydrometeor species for secondary ice (section 2e). This allows us to track activated INP and quantify the relative mass and number fractions of primary versus secondary ice at any given grid point throughout the simulation. For secondary ice, snow, and graupel, identical size distributions and habit characterizations are assumed as for primary ice listed under Table 2. Different experiments are conducted considering both SIP mechanisms in isolation or conjunction. Several studies (Sotiropoulou et al. 2020, 2021a,b) have shown BR to be governed by assumptions in RF, which remains unconstrained from observations. We thus include sensitivity experiments with RF ranging between 0.1 and 0.4. All numerical experiments are summarized in Table 1.

TABLE 2. Power-law coefficients for the maximum diameter $D(x) = ax^b$ and terminal fall velocity $v(x) = \alpha x^\beta$ of each hydrometeor type. As in Seifert and Beheng (2006), the mass–size relationship and terminal fall velocity are expressed in terms of mass $x$. The $\nu$ and $\mu$ are the parameters of the generalized Γ-distribution $f(x) = Ax^\nu \exp-\lambda x^\mu$, where $A = (\mu N/\{\Gamma[(\nu+1)/\mu]\})\lambda^{(\nu+1)/\mu}$ and $\lambda = (\{\Gamma[(\nu+1)/\mu]/\Gamma[(\nu+2)/\mu]\}\overline{x})^{-\mu}$.

| Type | $a$ | $b$ | $\alpha$ | $\beta$ | $\nu$ | $\mu$ |
|---|---|---|---|---|---|---|
| Cloud | 0.124 | 1/3 | $3.75 \times 10^5$ | 2/3 | 1 | 1 |
| Rain | 0.124 | 1/3 | 114.014 | 0.234 | 0 | 1/3 |
| Planar ice | 0.835 | 0.39 | 27.7 | 0.216 | 0 | 1/3 |
| Dendridic snow | 2.4 | 0.455 | 8.8 | 0.15 | 0 | 0.5 |
| Graupel | 0.15 | 0.323 | 32.0 | 0.18 | 1 | 1/3 |

## 4. SIP Impact on cloud micro- and macrophysics

Here, we discuss the impact of DS and BR parameterizations as well as their combined effect on simulated cloud micro- and macrophysical cloud properties. A summary of these results is provided in terms of averaged quantities for $n_d$, $n_i$, lwc, and iwc in Table 3. These spatiotemporal averages, like all time-averaged quantities, have been obtained following the first 4 h of simulation time, which were disregarded as spinup.

Following model spinup, the cloud continues to rise, while the mean cloud depth remains largely unchanged (maximum instantaneous deviation of at most 10%; Fig. 2). This results in the upward shift by around 250 m of all simulated thermodynamic and cloud profiles with respect to the observations (Fig. 1). Despite the upward shift in boundary layer height, the shape of the lwc profile (Fig. 1c) and in-cloud mean lwc (Table 3) are well captured by the simulations.

However, the overestimated deepening does introduce a cloud-top temperature bias of −2.5°C, which in theory impacts simulated ice nucleation and ice-phase growth rates. We accounted for the bias in immersion freezing rates in our INP specifications. These were chosen to match observed INP concentrations over the simulated in-cloud temperature range (section 3b). Meanwhile, the temperature bias alone accounts for an underestimation of depositional ice-phase growth rates near cloud top by 17%. This is well within the much larger uncertainty range introduced by other unconstrained factors such as ice crystal habit, secondary ice mechanisms, and SIP parameterization formulations. A more extensive discussion of uncertainty and its implications for the conclusions of this study is provided in section 6.

Consistent with previous studies (e.g., Fridlind et al. 2007; Possner et al. 2017; X. Zhao et al. 2021), we find that simulated $n_i$ (Table 3) and iwc (Fig. 1d) are underestimated by up to an order of magnitude in simulations without additional SIP processes outside the typical Hallet–Mossop temperature range. However, given the large uncertainty of the iwc measurement (discussed in section 3a), differences in mass are at best a very weak

TABLE 3. Time-averaged, in-cloud mean values ±1 standard deviation of $n_d$, $n_i$, lwc, and iwc of the observations obtained during flights on 9 Oct (Flight 1009) and 10 Oct (Flights 1010a and 1010b) 2004 (McFarquhar et al. 2007) in comparison with results from all performed sensitivity experiments (Table 1). Numbers in parentheses for $n_i$ and iwc denote the relative SIP contributions.

| | $n_d$ (cm$^{-3}$) | $n_i$ (L$^{-1}$) | lwc (gm$^{-3}$) | iwc (gm$^{-3}$) |
|---|---|---|---|---|
| Observations | | | | |
| Flight 1009 | 72.21 ± 34.32 | 1.41 ± 3.02 | 0.36 ± 0.22 | 0.022 ± 0.019 |
| Flights 1010a and 1010b | 24.72 ± 12.31 | 0.44 ± 0.57 | 0.25 ± 0.16 | 0.018 ± 0.020 |
| Simulations | | | | |
| *PROGINP_ctl* | 32.95 ± 8.32 | 0.13 ± 0.08 (<0.01%) | 0.29 ± 0.17 | 0.003 ± 0.003 (<0.1%) |
| *PROGINP_RF02* | 33.10 ± 8.31 | 0.13 ± 0.09 (10.0%) | 0.29 ± 0.16 | 0.004 ± 0.005 (3.3%) |
| *PROGINP_RF03* | 32.85 ± 8.27 | 0.16 ± 0.19 (35.2%) | 0.28 ± 0.16 | 0.006 ± 0.007 (12.0%) |
| *PROGINP_RF04* | 35.67 ± 9.07 | 102.00 ± 314.04 (>99.99%) | 0.28 ± 0.17 | 0.066 ± 0.142 (96.0%) |
| *PROGINP_DS* | 33.00 ± 8.31 | 0.67 ± 1.05 (86.6%) | 0.27 ± 0.16 | 0.014 ± 0.024 (64.2%) |
| *PROGINP_RF01_DS* | 32.86 ± 8.16 | 0.75 ± 1.24 (88.0%) | 0.26 ± 0.16 | 0.015 ± 0.028 (68.5%) |
| *PROGINP_RF02_DS* | 32.84 ± 8.29 | 0.94 ± 1.74 (90.4%) | 0.26 ± 0.16 | 0.017 ± 0.031 (72.3%) |
| *PROGINP_noPRIM* | 32.87 ± 8.16 | 0.85 ± 1.30 (95.4%) | 0.27 ± 0.16 | 0.016 ± 0.028 (85.4%) |
| *PROGINP_10INP* | 33.75 ± 7.82 | 0.60 ± 0.43 (<0.01%) | 0.26 ± 0.15 | 0.013 ± 0.017 (<0.01%) |
| *PROGINP_2xCCN* | 79.29 ± 14.28 | 0.15 ± 0.11 (16.9%) | 0.34 ± 0.18 | 0.097 ± 0.008 (4.9%) |
| *RELINP_DS* | 32.79 ± 8.27 | 0.75 ± 1.14 | 0.27 ± 0.16 | 0.015 ± 0.03 |
| *RELINP_RF01_DS* | 32.70 ± 8.32 | 0.87 ± 1.36 | 0.27 ± 0.16 | 0.016 ± 0.033 |
| *RELINP_RF02_DS* | 32.31 ± 8.27 | 1.26 ± 2.36 | 0.26 ± 0.16 | 0.020 ± 0.042 |

constraint. Note that the small, though nonzero, fraction of secondary ice in *PROGIN_ctl* is generated by small rates of rime splintering through Hallet–Mossop. The impact of the implemented BR and DS mechanisms in simulations with a prognostic temperature-dependent INP budget (section 2b), is presented in the following sections.

### a. *BR only*

We first consider the impact of the BR mechanism in isolation. Ice crystal fragmentation through BR has been shown to increase $n_i$ substantially in warmer supercooled clouds (Sotiropoulou et al. 2020). During M-PACE, simulated and observed cloud-top temperatures are at or below −17° and −15°C, respectively. At these temperatures, we do not simulate a stable MPC considering only BR in addition to Hallet–Mossop rime splintering.

BR efficacy is constrained by the number of collisions between ice-phase hydrometeors and the number of fragments generated by each collision [$n_{\mathrm{br}}$ defined in Eq. (8)]. The latter is known to be a strong function of the assumed RF that remains as of yet unconstrained from observations. For a specified RF of 0.2 (*PROGINP_RF02*) merely 10% (Table 3) of the mean $n_i$ stems from SIP, and simulated $n_i$ and iwc remain underestimated. Also, the time evolution of $n_i$ still closely follows that of *PROGINP_ctl* (Fig. 3a).

Increasing $n_{br}$ by increasing RF to 0.3 yields a moderate increase in vertically integrated $n_i$. Meanwhile, an increase in RF to 0.4 leads to a rapid increase in $n_i$ by two orders of magnitude within 2 h. As a result, the tiwp (Fig. 4e) increases fivefold at the expense of the lwp (Fig. 4a), which drops below 10 gm$^{-2}$. Thus, following peak BR rates the cloud is almost fully glaciated within a short period of time.

In *PROGINP_RF04* a self-amplifying loop of fragmentation is triggered once the vertically integrated SIP production rate increases above 100 m$^{-2}$ s$^{-1}$ (Fig. 3b). While an RF of 0.4 may be unrealistic, analyzing the instability of these results is still of interest since much larger SIP rates are simulated with active DS (Fig. 3b). Yet, the simulation remains stable, which will be discussed in the following section. The self-amplifying loop consists of BR fragmentation increasing $n_i$, which in turn increases the number of ice–ice collisions and enhances fragmentation. This process is eventually limited in the absence of sufficient cloud water.

Overall, these results show that an increased and sustained level of SIP in the M-PACE mixed-phase cloud deck is unlikely to be achieved through BR alone. Simulated $n_i$ either remain biased negatively (low) (Fig. 5a) because vertically integrated BR rates remain below 100 m$^{-2}$ s$^{-1}$ (Fig. 3b) or exceed observed high percentiles of $n_i$ by an order of magnitude (Fig. 5a), which triggers partial cloud glaciation.

### b. *DS only*

In contrast to the BR-only results discussed in the previous paragraphs, considering only DS (*PROGINP_DS*), in addition to Hallet–Mossop, leads to a simulated sustained increase in $n_i$ (Fig. 3a) and tiwp (Fig. 4e). The median and spatiotemporal average $n_i$ are increased from 0.1 l$^{-1}$ and 0.13 l$^{-1}$ in *PROGINP_ctl* to 0.25 and 0.67 l$^{-1}$ in *PROGINP_DS* respectively. The larger proportional increase in domain-mean $n_i$ is due to a disproportional increase in high-percentile $n_i$ in *PROGINP_DS*. Indeed, the observed peak $n_i$ concentration of 2.2 l$^{-1}$ is only captured in simulations including DS and remains underestimated by an order of magnitude in *PROGINP_ctl* and stable BR-only simulations.

The temporal evolution of $n_i$ is governed by the simulated DS rates (Fig. 3c), which in turn follow the temporal evolution of the simulated rwp (Fig. 4b) and its spatial distribution, which is discussed further in the following section. A stabilizing feedback loop develops where periods of increased rain intensity amplify DS rates, which in turn increases the sink on

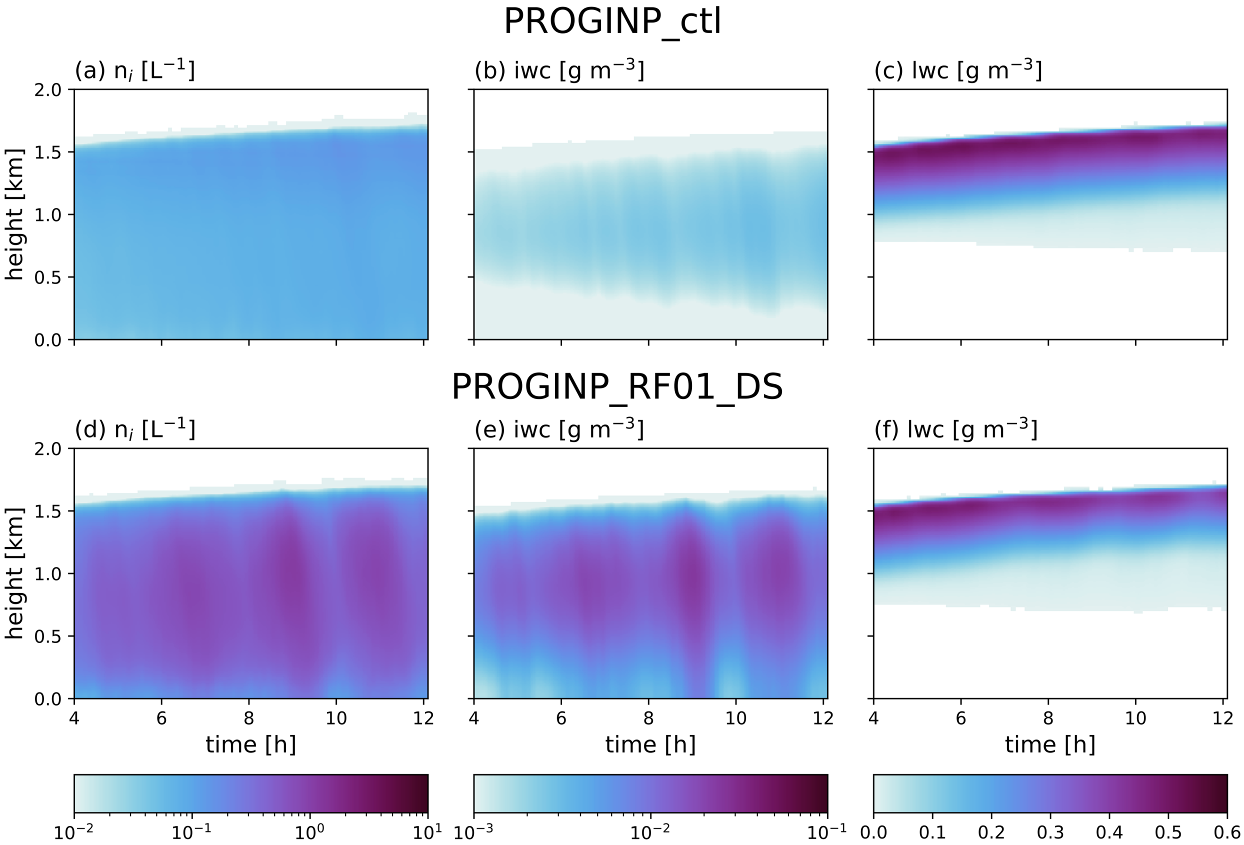

FIG. 2. Hovmöller diagrams of (a),(d) ice crystal number concentration $n_i$; (b),(e) total ice water content iwc; and (c),(f) liquid water content lwc for (top) the control simulation *PROGINP_ctl* and (bottom) the *PROGINP_RF*01*_DS* sensitivity experiment specified in Table 1.

cloud and rainwater content through efficient WBF growth of the small generated ice fragments, which contribute over three-quarters of the total ice mass (Table 3).

As a consequence, both rwp and DS rates decrease, until the rain recovers and the next oscillation is triggered. Throughout the simulation the mean rwp oscillates around 5 gm$^{-2}$. During time periods with a relative rwp increase, a larger number of sufficiently large drops is available as efficient shatterers upon freezing. Figure 2a in X. Zhao et al. (2021) shows that already small raindrops (radius of 60 $\mu$m) are sufficient following the Phillips et al. (2017) parameterization.

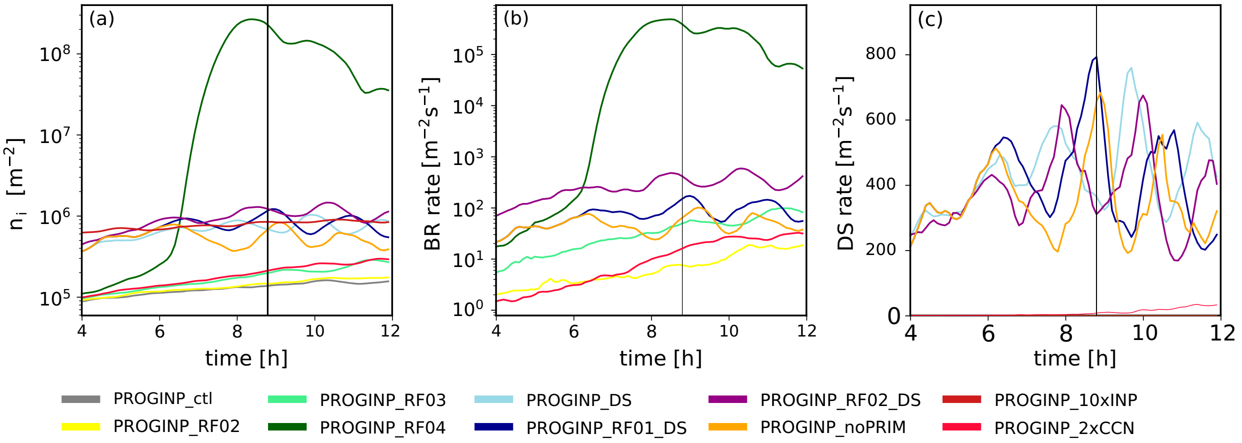

FIG. 3. Time series of (a) horizontally averaged and vertically integrated $n_i$, along with instantaneous vertically integrated and horizontally averaged (b) BR and (c) DS SIP rates. Results are shown for all *PROGINP* runs listed in Table 1. The vertical line marks the time stamp for which the instantaneous spatial variability is analyzed in Fig. 6, described in more detail below.

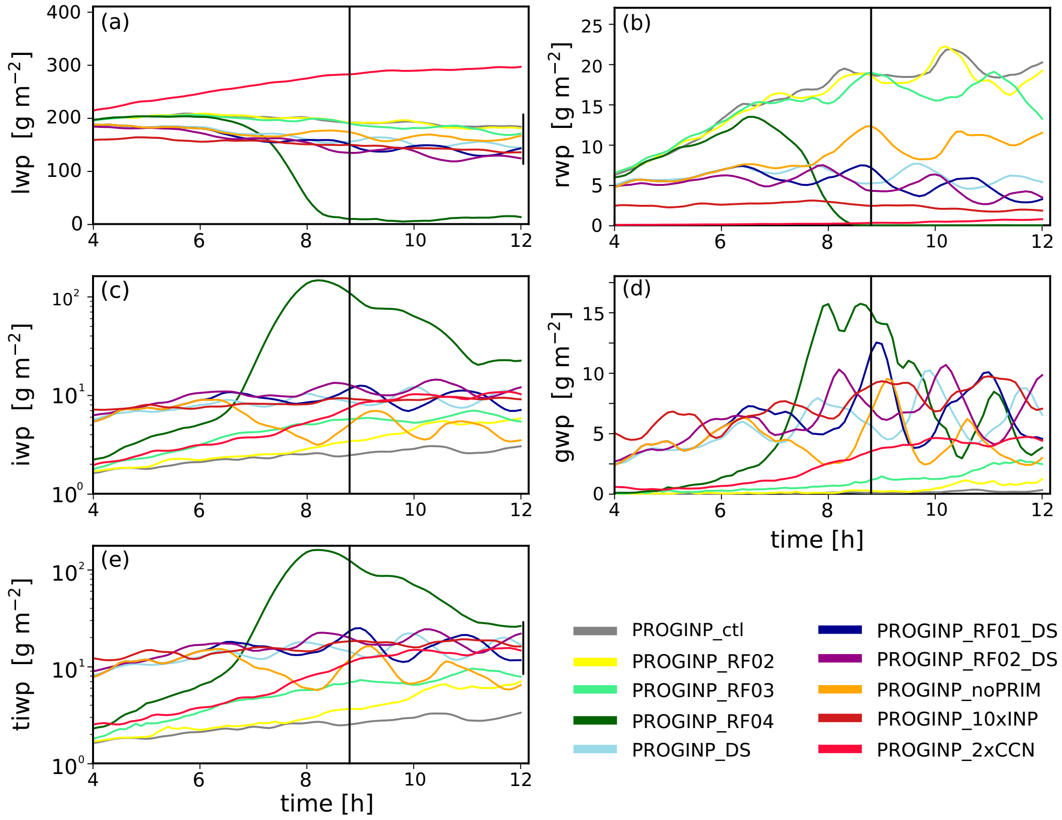

FIG. 4. Time series of field mean values of (a) lwp, (b) rainwater path rwp, (c) combined ice + snow water path (iwp), (d) graupel water path gwp, and (e) tiwp of all *PROGINP* simulations (Table 1). The vertical bar (black) added at the end of the time series in (a) and (e) denotes the observed range. The vertical line (between 8 and 10 h) marks the time stamp for which the instantaneous spatial variability is analyzed in Fig. 6, below.

While good agreement is found between observed and simulated mean and peak $n_i$ statistics, the simulated variability in $n_i$ is larger than observed. The simulated interquartile spread (Fig. 5a) in $n_i$ (scaled by the median $n_i$ concentration) is 1.5 times the observed scaled interquartile spread of 165%, and over 3 times the simulated spread in *PROGINP_RF*02. This suggests that DS is associated with a larger spatiotemporal variability than BR in our simulations. This is discussed further in the following section, which looks at the spatial covariability between SIP rates and macrophysical cloud properties in more detail.

In summary, we find that *PROGINP_DS* captures in situ $n_i$ observations and remote sensing lwp, and tiwp retrievals. This further corroborates previous findings that the parameterized DS dominates SIP rates over contributions from the BR parameterization during M-PACE (X. Zhao et al. 2021).

### *c. DS and BR combined*

The combined efficacy of DS and BR is assessed in simulations considering DS and BR simultaneously. This also includes a contrasting discussion between both SIP process rates in terms of their spatial heterogeneity, impact on, and covariability with micro- and macrophysical cloud properties.

The efficacy of the BR parameterization in conjunction with DS is assessed for two different prescribed RFs of 0.1 (*PROGINP_RF*01*_DS*) and 0.2 (*PROGINP_RF*02*_DS*). Overall, the inclusion of BR in simulations with DS acts to amplify SIP. Averaged $n_i$ is initially increased (Table 3) from 0.67 $\mathrm{l}^{-1}$ (*PROGINP_DS*) to 0.75 $\mathrm{l}^{-1}$ (*PROGINP_RF*01*_DS*) and to 0.94 $\mathrm{l}^{-1}$ (*PROGINP_RF*02*_DS*). Both simulations are stable and yield ice-phase characteristics (iwc and $n_i$) in the observed range.

We simulate the same oscillatory behavior in *PROGINP_RF*01*_DS* as in *PROGINP_DS* between periods of increased rwp (Fig. 4b) and DS (Fig. 3c), versus periods of increased tiwp (Fig. 4e) and temporarily lower SIP rates. This changes in *PROGINP_RF*02*_DS*. In this simulation vertically integrated BR rates temporarily exceed 300 $\mathrm{m}^{-2}\,\mathrm{s}^{-1}$ and dampen the relationship between the availability of sufficiently numerous, and sufficiently large, drizzle-sized drops and SIP. This shows that in combination with DS, larger BR rates can be sustained within a stable (albeit biased) MPC, where similarly large BR rates triggered partial glaciation in BR-only simulations (section 4a).

This difference in behavior between BR-only, and combined DS + BR runs can be explained by looking at the spatial heterogeneity of DS and BR. Both SIP processes occur predominantly

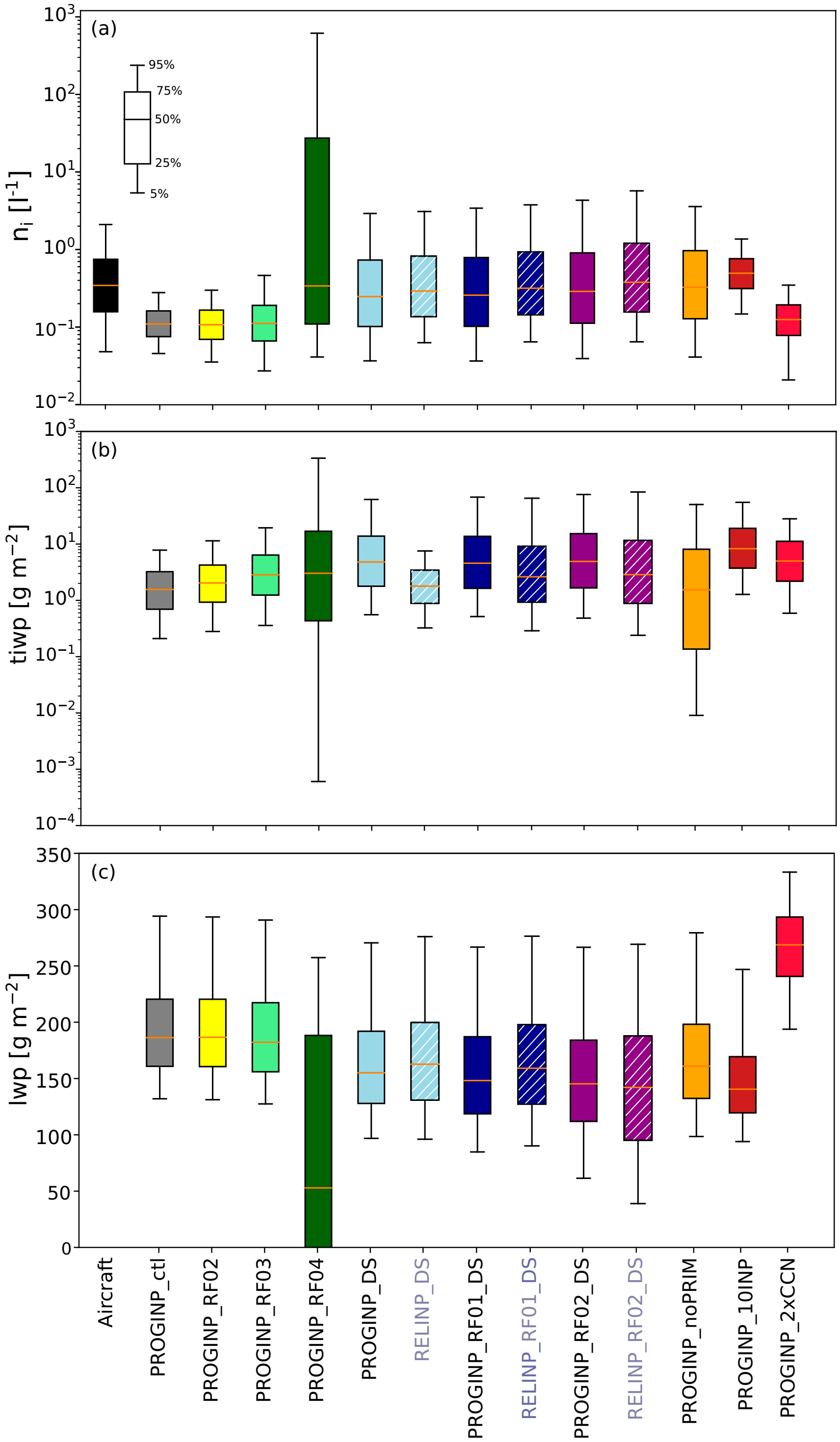

FIG. 5. Box plot for (a) in-cloud ice number concentration $n_i$, (b) total ice water path tiwp, and (c) liquid water path lwp. Results are shown for all sensitivity experiments summarized in Table 1.

within the detraining convective regions at the boundary layer top. These regions are supplied by moisture from the detraining convective cores (indicated by regions of lwp $> 300$ gm$^{-2}$), and high values in tiwp and rwp (Fig. 6). The figure shows the instantaneous (time of snapshot marked by vertical black lines in Figs. 3 and 4) spatial cloud field and SIP variability.

It should be noted that areas of increased water paths and SIP rates are spatially collocated and about 4 times as large as

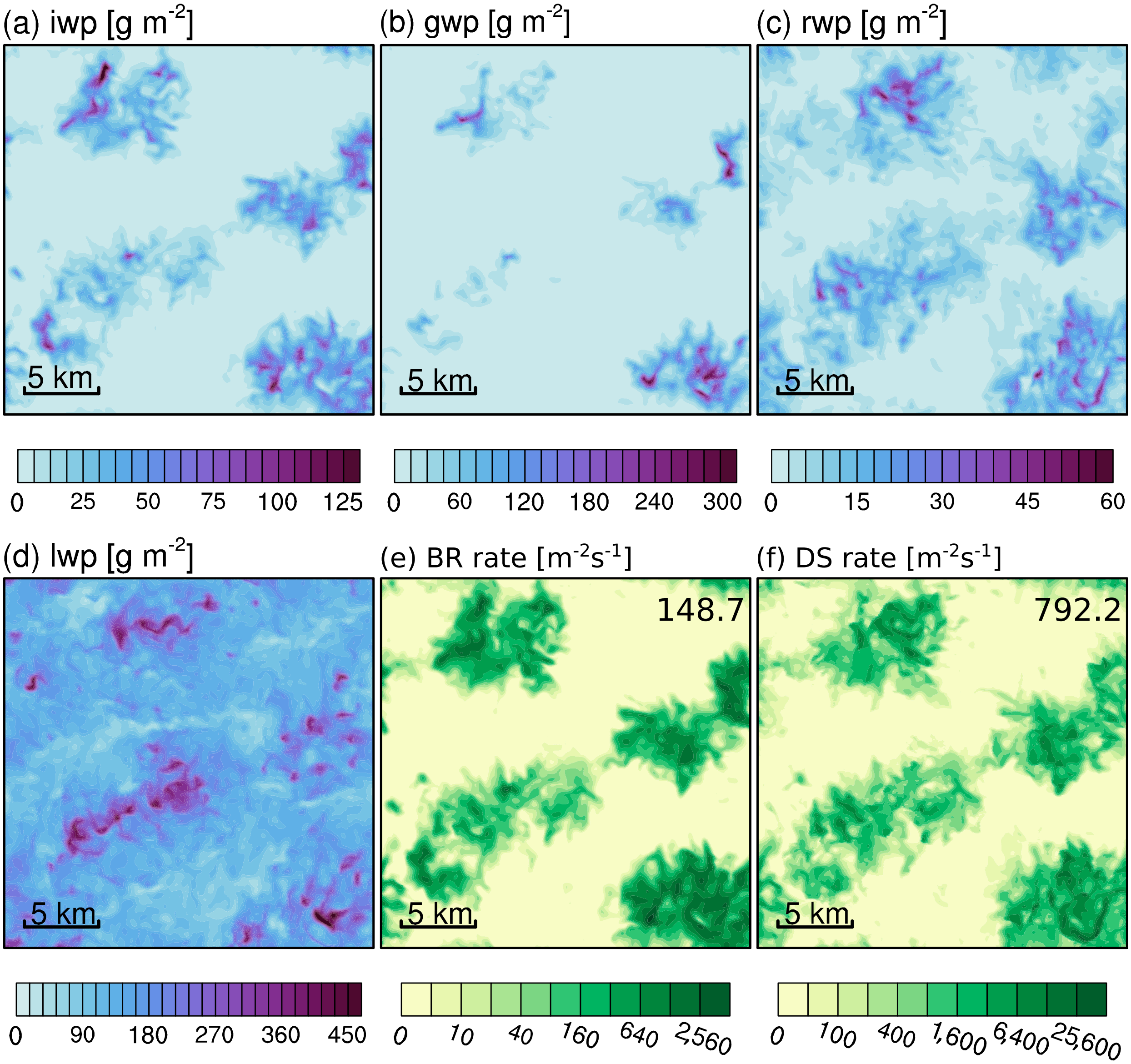

FIG. 6. Spatial variability of instantaneous fields for (a) ice water path iwp, (b) graupel water path gwp, (c) rainwater path rwp, (d) liquid water path lwp, (e) BR rate, and (f) DS rate from *PROGINP_RF*01_*DS*. The instantaneous spatial variability is shown at the time of the DS rate maximum (Fig. 3c) during which BR rates are also high (Fig. 3b).

the area covered by the updraft cloud core structures themselves. Cloud cores occupy about 10% of the simulation domain as indicated by the vertical distribution in liquid cloud fraction below the stratiform cloud base (Fig. 7b). The shattering of freezing raindrops triggers significant BR rates at low RF, due to the increase in collision frequency in the presence of more numerous ice crystals. The animation of *PROGINP_RF*01_*DS* provided in the online supplemental material of this paper shows that the instantaneous structure shown in Fig. 6 is representative of the last 6 h of the simulated cloud evolution.

Both SIP rates are highest around the cloud base, where the largest raindrops occur increasing DS efficacy, and ice crystals grow rapidly through depositional growth and riming to facilitate additional fragmentation through BR. Thus $n_i$ increases from cloud top to cloud base in simulations with discernible SIP contributions to the overall $n_i$ budget. This negative slope is consistent with the observations and in clear contrast to the positive slope imposed by primary nucleation (Fig. 7a). As in X. Zhao et al. (2021), we regress the observed $n_i$ against height and obtain a negative slope between cloud top and cloud base from the observations. Immersion freezing rates are confined to the cloud-top region and consequently $n_i$ decreases upon sedimentation through collision–coalescence. Consequently, positive slopes in $n_i$ are simulated in all simulations governed by primary nucleation (i.e., *PROGINP_ctl*, *PROGINP*_10*INP*, and *PROGINP_RF*02).

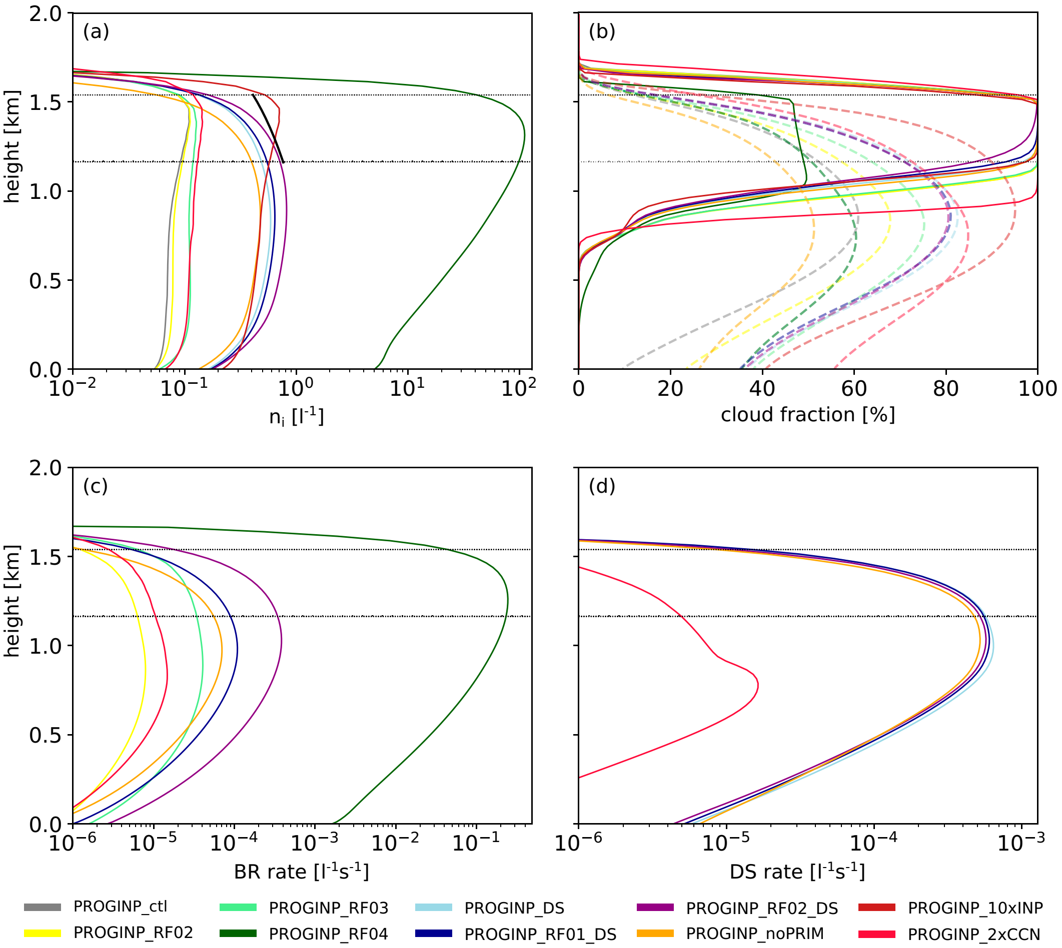

FIG. 7. Vertical profiles of domain mean (a) $n_i$, (b) liquid (solid line) and ice (dashed line) cloud fraction, (c) DS and (d) BR SIP rates for all *PROGINP* simulations (Table 1). The averaged cloud-top height and cloud-base height (horizontal black dashed lines) representative for all simulations other than *PROGINP_RF*03 and *PROGINP_RF*04 are added to aid interpretation.

In summary, these experiments show that in terms of mean $n_i$, its spatiotemporal variability, and vertical slope, only simulations including DS reproduce liquid- and ice-phase cloud macro- and microphysical properties. It further demonstrates how vertically resolved observations or retrievals of $n_i$ can indirectly help to constrain the occurrence and potential importance of SIP in single-layer MPCs more generally.

## 5. Importance of primary nucleation

Previous studies have emphasized the importance of INP recycling for primary nucleation during M-PACE (Fridlind et al. 2007; Fan et al. 2009; Solomon et al. 2015; Possner et al. 2017; Fu et al. 2019). Here, we revisit the importance of primary nucleation in simulations that best capture the distribution of observed $n_i$ and consist of at least 87% secondary ice and snow (Table 3) that contain at least 64% of the total ice mass. We thus pose the question if SIP, once triggered, is self-sustaining and can maintain an MPC deck over several hours.

This is explored in *PROGINP_noPRIM* (Table 1), where primary nucleation is artificially turned off following model spinup. This experiment also allows us to assess the potential importance of continued primary nucleation in SIP-dominated MPCs. We find that the median $n_i$ (Fig. 5a) slightly increases from 0.26 $l^{-1}$ (*PROGINP_DS_RF*01) to 0.32 $l^{-1}$ (*PROGINP_noPRIM*). Meanwhile, peak concentrations and interquartile spread normalized by median concentrations between the two simulations are comparable. This suggests that MPCs governed by SIP are not only self-sustaining over at least the remaining simulated 8 h, but that SIP efficacy increased in the absence of primary nucleation.

Primary nucleation predominantly occurs at the cloud top, where the competition for water vapor between the ice and the liquid phase is now reduced in *PROGINP_noPRIM*. As a consequence the simulated lwp and rwp increase. As discussed in the previous section, DS is efficient during periods of high rwp. Consequently, SIP rates (predominantly DS, but also BR) increase.

In contrast, a decrease in domain mean $n_i$, DS, and BR rate profiles (Fig. 7) and their respective time evolution (Fig. 3) is

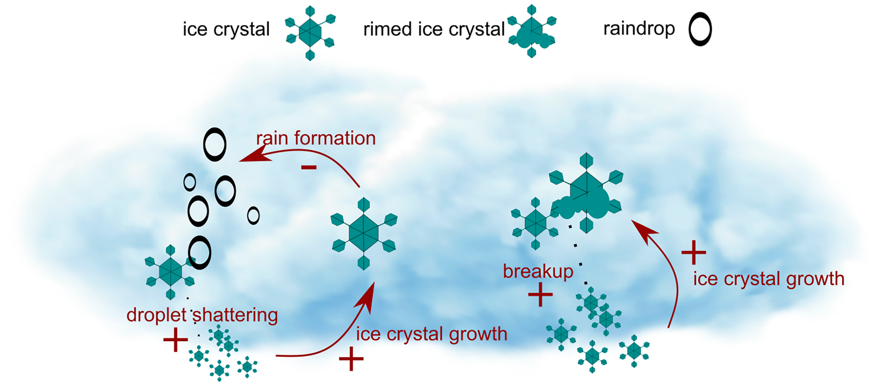

FIG. 8. Schematic illustrating feedback loops for DS and BR mechanisms governing simulated cloud evolution.

simulated. This is due to the substantial decrease in simulated ice-cloud fraction (Fig. 1b) in *PROGINP_noPRIM* with respect to *PROGINP_DS_RF*01. Thus, the decrease in ice-cloud fraction overcompensates the increase in in-cloud properties.

This sensitivity experiment shows that, at least in cloud-resolving ICON simulations, primary nucleation dampens SIP rates dependent on rain formation due to the resulting stress on liquid condensate from rapidly growing, freshly nucleated ice crystals. Meanwhile, the simulated ice cloud fraction remains dependent on primary nucleation and INP recycling. INP released upon sublimation are advected upward through the updraft cores and laterally re-entrained into the cloud layer where they renucleate in anvil-like structures at the cloud top.

Given the seemingly sustained importance of primary nucleation, we conducted three additional experiments *RELINP_DS*, *RELINP_DS_RF*01, and *RELINP_DS_RF*02 to investigate whether simulated ice-phase, or liquid-phase, properties were impacted by using a simpler, albeit numerically cheaper, implementation for immersion freezing (see section 2a). The simulated domain mean $n_i$ and iwc averages increased by 21% and 10% respectively (Table 3). However, this increase in domain mean quantities largely stems from the tails of the distributions, which are otherwise statistically invariant from one another (a Bhattacharyya distance of 0.01 is computed between all three sets of experiments, where 0 indicates complete overlap and $\infty$ indicates distinctness). Thus, these simulations suggest that a simpler form of INP parameterization may be sufficient as long as the climatological vertical and seasonal variability of the prescribed INP profile is captured.

One final experiment was conducted, which further substantiates the contribution of SIP to observed $n_i$. In *PROGINP_*10*INP*, the INP concentration was scaled up by a factor 10 to close the gap to $n_i$ observations by only considering primary nucleation (Table 3).

This increases time-averaged iwc estimates to within the observed range (Table 3). Meanwhile, the variability in $n_i$ is considerably underestimated (Fig. 5a). In particular, peak concentrations in $n_i$ are missed. This is due to the spatially more homogeneous distribution of immersion freezing near the cloud top. This further supports analyses that use the spatial heterogeneity of $n_i$ and INP to detect the presence of SIP in MPCs (e.g., Pasquier et al. 2022).

## 6. Implications and limitations

In this study, we investigate the impact of two previously tested SIP parameterizations (Phillips et al. 2017, 2018) on simulated cloud properties and boundary layer structures constrained by M-PACE in situ observations ($n_i$, $n_d$, and INP), and ground-based remote sensing retrievals (iwc and lwc). This particular case was chosen due to the known discrepancy between INP and $n_i$ observations even when the impact of inlet shattering is accounted for (Jackson and McFarquhar 2014).

We find that BR alone is either insufficient to match ice-phase observations, or triggers partial cloud glaciation in the M-PACE MPC deck (section 4a). This has now been shown across multiple models and resolutions (Fridlind et al. 2007; Fu et al. 2019; M. Zhao et al. 2021; Sotiropoulou et al. 2021a). We attribute this to a self-amplifying loop of simulated ice fragmentation summarized in Fig. 8. During M-PACE conditions, the secondary ice fragments grow rapidly through depositional growth (WBF and water subsaturated growth) and riming and are quickly ready to fragment again. This pathway is especially strong in this simulated temperature regime (cloud-top temperature at or below −15°C), where WBF growth is particularly strong due to the large difference between the ice and liquid saturation curves as compared with warmer temperatures.

Meanwhile, stable rates of fragmentation at the order of 100 $\mathrm{m^{-2}\ s^{-1}}$ are simulated in simulations including DS (DS-only and DS + BR runs). In these simulations, a stable loop of amplification for $n_i$ is entered. In our simulations, the growth of the newly generated secondary ice crystals acts to reduce its source of generation, namely the growth of large drizzle drops (Fig. 8). This results in a stable out-of-sink oscillation between rwp and $n_i$ (Figs. 4b and 3a respectively). Note that this will change in boundary layers where the melting line is crossed above, or just below, the cloud base. Under these conditions, rain production is not just governed by pure-liquid processes, which may alter the operation of this feedback loop.

Our sensitivity experiments also demonstrate the explicit link between mesoscale cloud organization and simulated SIP rates. SIP is confined to 48% of the entire cloud deck and clusters around regions of detraining shallow convection. Individual studies (Eirund et al. 2019; Tornow et al. 2021; Karalis et al. 2022) link mesoscale cloud dynamics and ice production in the context of potential shifts in mesoscale patterns. Yet, a systematic quantitative assessment of these processes, from observations and cloud-resolving model simulations, remains to be attained. Spatial coherence through mesoscale organization may also impact quantitative assessments of the importance of SIP in MPCs. Extrapolating from these results, SIP may be confined to just the convective cores in conditions characterized by weaker surface fluxes and weaker detrainment of moisture in the overlying decoupled stratocumulus cloud. Thus, SIP may only occur within 10% of the entire cloud layer. Nonetheless, the lwp and thus the radiative properties of the entire cloud field may be impacted by these 10%.

Uncertainties with respect to SIP mechanisms, and their implementation in numerical models, remain high. These simulations highlight how high-resolution simulations in combination with detailed cloud micro- and macrophysical observations can be used to enhance our understanding of these mechanisms and to better understand their potential climatological importance. However, given these uncertainties, several limitations remain within this study, which we discuss in the following paragraphs.

First, we do not take the freezing and subsequent shattering of raindrops upon freezing (Hobbs and Alkezweeny 1968; Lauber et al. 2018) into account. This alternate mechanism has been proposed to contribute, and perhaps even dominate SIP and may impact the conclusions of this study. However, based on previous assessments, we do not simulate sufficiently large raindrops and a too cold cloud base, for efficient fragmentation to occur via this mechanism (Sullivan et al. 2018).

However, the efficacy of DS is a clear function of the available rain as shown by the *RROGINP_2xCCN* experiment in comparison with the *PROGINP_DS_RF*01 simulation. The increase in simulated $n_d$ consistent with the upper bound of $n_d$ measurements leads to a substantial reduction in the SIP contribution to the simulated cloud ice from 88% to 17% (Table 3). Thus, our conclusions with respect to the importance of DS are subject to the existence of drizzle and convective mesoscale organization. Drizzle rates themselves cannot be constrained from available observations in the MPC regime, as spherical hydrometeors observed by the cloud particle imager may be liquid or frozen (McFarquhar et al. 2007). However, the existence of drizzle is very likely given the mesoscale roll cloud organization, which is driven by precipitation.

Second, BR rates are a strong function of the rimed mass fraction and crystal habit characterization of an evolving population of crystals. Waitz et al. (2022) present first constraints on the number fraction of lightly or heavily rimed crystals of Arctic MPCs, but the rimed mass fraction remains virtually unconstrained from observations. As in previous work, we attempt to mitigate this by conducting sensitivity experiments with respect to RF. However, changes in vertical and horizontal spatiotemporal variability of RF, and its impact on BR efficacy, cannot be assessed in this manner.

The same holds for crystal habit characterizations, which in reality evolve throughout the cloud and its lifetime. Several studies have shown that ice crystal shape assumptions, and spectral shape assumptions, of the ice-phase size distributions can strongly impact MPC processes by altering simulated ice growth and ice sedimentation rates (Avramov et al. 2011; Sulia et al. 2014; Ovchinnikov et al. 2014; Zhang et al. 2022). Thus the hypotheses formulated in this study require further testing and substantiation across a variety of cases where RF and crystal habit characterizations are constrained.

Third, process interactions are investigated in a two-moment bulk microphysics scheme, where freshly nucleated ice fragments are treated with the same monomodal size distribution as larger aged ice crystals. While bulk schemes allow us to conduct high-resolution simulations on mesoscale domains to investigate the interactions between cloud physics and dynamics, the homogenization of the size distribution, imposed by the structure of the bulk scheme, will impact the assessed efficacy of SIP mechanisms and needs to be further constrained in combination with more detailed microphysical modeling.

Fourth, we use a simplified treatment of immersion freezing in these simulations. The applied parameterization in this study only takes a very crude representation of in-cloud INP processing into account and neglects details on aerosol composition. Simulated immersion freezing rates in MPCs are an exponential function of temperature. While we have mitigated the negative bias in simulated cloud-top temperature in our simulation setup, we still do not resolve small-scale temperature fluctuations, which may substantially impact simulated immersion freezing rates. Thus, to further substantiate our hypothesis on the seemingly reduced importance of continued primary nucleation once SIP is established, the in-cloud processing of INP, and the importance of small-scale temperature fluctuations for the overall INP budget of a given cloud field, would need to be better constrained in a combined effort of new observations and high-resolution modeling.

Last, the simulated boundary layer is overestimated in its vertical extent by 250 m. Test simulations (not shown) with lower prescribed SST (and lower surface fluxes), or increased rates of subsidence, did not deepen as much as in *PROGINP_ctl*. However, simulations with increased subsidence suppressed all shallow convection resulting in a homogeneous stratocumulus deck not resembling the observed roll structure. In agreement with our hypothesis, very little SIP was simulated in the absence of mesoscale organization. Meanwhile, simulations with lower prescribed SST were associated with substantial low biases in boundary layer temperature (humidity) of several degrees (up to 0.5 g $\mathrm{kg}^{-1}$).

As the boundary layer gradually continues to deepen during the simulation, the cloud deck gradually shifts upward at constant geometrical thickness. Meanwhile, the convective cloud base remains unchanged (denoted by the onset of contours in Fig. 2c). Consequently, the convective cloud cores are overestimated in their vertical extent. This could bias simulated rain rates and thus the efficacy of DS as currently parameterized. However, rain production is also found to be a strong function of $n_d$ via simulated autoconversion rates. As cloud base rain rates are unconstrained from observations during M-PACE, further research is needed to corroborate these findings.

Overall, many uncertainties remain, due to the incomplete mechanistic understanding of SIP, insufficiently constrained parameterizations, and ice-phase properties. It is thus not possible to generalize from the results of this study. However, we were able to test the sensitivity of the simulated MPC cloud deck to two proposed SIP parameterizations in ICON and to formulate process hypotheses, which are summarized in our conclusions.

## 7. Conclusions

Many uncertainties remain with respect to the physics of SIP mechanisms and their implementation via empirical formulations into bin and bulk microphysical models. This study explores the interactions between different primary nucleation and SIP parameterizations in idealized cloud-resolving ICON simulations. We quantify the relative impact of different parameterization combinations (see Table 1) on averaged ice and liquid cloud properties, and their spatiotemporal heterogeneity. Our findings and formulated hypotheses based on this analysis can be summarized as follows:

- The $n_i$ enhancement through SIP can close the gap between measured and simulated $n_i$ concentrations during M-PACE. In particular, only simulations including DS (potentially amplified by BR) maintain a stable rate of sufficient fragmentation in our simulations.
- A stable MPC can be maintained in the absence of continued primary nucleation once SIP is established. Meanwhile, the areal extent of the ice-containing cloud fraction remains dependent on primary nucleation.
- Simulated SIP rates and mesoscale cloud organization are strongly linked in our simulations. This indicates that such links should be considered in quantitative assessments of the impact of SIP on MPCs in terms of area percentage contributions.
- Sensitivity studies using a computationally more efficient prognostic parameterization of primary nucleation based on relaxed INP concentrations are statistically invariant from simulations considering the full prognostic INP budget.

Given the uncertainties discussed at length in the previous section, we are unable to generalize from these simulations alone. For future work, we argue that (i) process hypotheses will need to be confirmed in property-based microphysics schemes that represent the evolution of rimed fraction and crystal habits, rather than imposing time-invariant assumptions, and that include a more physical representation of aerosols nucleating via immersion freezing, and (ii) longer-term, cloud-resolving simulations are needed to corroborate the significance of these findings and their importance for Arctic MPCs more generally.

*Acknowledgments.* This work was funded by the Federal Ministry of Education and Research (BMBF) under the “Make our Planet Great Again–German Research Initiative”, grant 57429624, implemented by the German Academic Exchange Service (DAAD) and by the Hans Ertel Centre for Weather Research of DWD (fourth phase), grant 4823DWDP7. This work used resources of the Deutsches Klimarechenzentrum (DKRZ) granted by its Scientific Steering Committee (WLA) under projects bb1137 and bb1358. We also thank Prof. S. Sullivan for sharing initial SIP routines for DS and BR in ICON and Prof. Z. Wang for sharing the M-PACE MICROBASE data product for lwc and iwc.

*Data availability statement.* All observations from the M-PACE campaign are publicly available through the ARM user facility (https://adc.arm.gov/discovery/; last access: 22 August 2022). The model datasets and modified code of the licensed ICON microphysics are stored at the German Climate Computing Center (DKRZ). All data are made available upon request, and all code modifications are shared with ICON license holders.

## REFERENCES

Avramov, A., and Coauthors, 2011: Toward ice formation closure in Arctic mixed-phase boundary layer clouds during ISDAC. *J. Geophys. Res.*, **116**, D00T08, https://doi.org/10.1029/2011JD015910.

Bergeron, T., 1935: On the physics of clouds and precipitation. *Proc. Fifth Assembly of the International Union of Geodesy and Geophysics*, Lisbon, Portugal, 156–180.

Beydoun, H., and C. Hoose, 2019: Aerosol-cloud-precipitation interactions in the context of convective self-aggregation. *J. Adv. Model. Earth Syst.*, **11**, 1066–1087, https://doi.org/10.1029/2018MS001523.

DeMott, P. J., and Coauthors, 2015: Integrating laboratory and field data to quantify the immersion freezing ice nucleation activity of mineral dust particles. *Atmos. Chem. Phys.*, **15**, 393–409, https://doi.org/10.5194/acp-15-393-2015.

——, and Coauthors, 2016: Sea spray aerosol as a unique source of ice nucleating particles. *Proc. Natl. Acad. Sci. USA*, **113**, 5797–5803, https://doi.org/10.1073/pnas.1514034112.

Dipankar, A., B. Stevens, R. Heinze, C. Moseley, G. Zängl, M. Giorgetta, and S. Brdar, 2015: Large eddy simulation using the general circulation model ICON. *J. Adv. Model. Earth Syst.*, **7**, 963–986, https://doi.org/10.1002/2015MS000431.

Eirund, G. K., U. Lohmann, and A. Possner, 2019: Cloud ice processes enhance spatial scales of organization in Arctic stratocumulus. *Geophys. Res. Lett.*, **46**, 14 109–14 117, https://doi.org/10.1029/2019GL084959.

Ervens, B., and G. Feingold, 2013: Sensitivities of immersion freezing: Reconciling classical nucleation theory and deterministic expressions. *Geophys. Res. Lett.*, **40**, 3320–3324, https://doi.org/10.1002/grl.50580.

Fan, J., M. Ovchinnikov, J. M. Comstock, S. A. McFarlane, and A. Khain, 2009: Ice formation in Arctic mixed-phase clouds: Insights from a 3-D cloud-resolving model with size-resolved aerosol and cloud microphysics. *J. Geophys. Res.*, **114**, D04205, https://doi.org/10.1029/2008JD010782.

Febvre, G., J.-F. Gayet, V. Shcherbakov, C. Gourbeyre, and O. Jourdan, 2012: Some effects of ice crystals on the FSSP measurements in mixed phase clouds. *Atmos. Chem. Phys.*, **12**, 8963–8977, https://doi.org/10.5194/acp-12-8963-2012.

Field, P. R., R. Wood, P. R. A. Brown, P. H. Kaye, E. Hirst, R. Greenaway, and J. A. Smith, 2003: Ice particle interarrival times measured with a fast FSSP. *J. Atmos. Oceanic Technol.*, **20**, 249–261, https://doi.org/10.1175/1520-0426(2003)020<0249:IPITMW>2.0.CO;2.

——, and Coauthors, 2017: Secondary ice production: Current state of the science and recommendations for the future. *Ice Formation and Evolution in Clouds and Precipitation: Measurement and Modeling Challenges*, *Meteor. Monogr.*, No. 58, Amer. Meteor. Soc., https://doi.org/10.1175/AMSMONOGRAPHS-D-16-0014.1.

Findeisen, W., 1938: Kolloid-meteorologische Vorgänge bei Niederschlagsbildung. *Meteor. Z.*, **55**, 121–133.

Fridlind, A. M., A. S. Ackerman, G. McFarquhar, G. Zhang, M. R. Poellot, P. J. DeMott, A. J. Prenni, and A. J. Heymsfield, 2007: Ice properties of single-layer stratocumulus during the Mixed-Phase Arctic Cloud Experiment: 2. Model results. *J. Geophys. Res.*, **112**, D24202, https://doi.org/10.1029/2007JD008646.

Fu, S., X. Deng, M. D. Shupe, and H. Xue, 2019: A modelling study of the continuous ice formation in an autumnal Arctic mixed-phase cloud case. *Atmos. Res.*, **228**, 77–85, https://doi.org/10.1016/j.atmosres.2019.05.021.

Giangrande, S., and M. Jensen, 2002: Continuous Baseline Microphysical Retrieval (MICROBASEPI2). Atmospheric Radiation Measurement, accessed 22 August 2022, https://doi.org/10.5439/1034923.

Hallett, J., and S. C. Mossop, 1974: Production of secondary ice particles during the riming process. *Nature*, **249**, 26–28, https://doi.org/10.1038/249026a0.

Hande, L. B., C. Engler, C. Hoose, and I. Tegen, 2016: Parameterizing cloud condensation nuclei concentrations during HOPE. *Atmos. Chem. Phys.*, **16**, 12 059–12 079, https://doi.org/10.5194/acp-16-12059-2016.

Heinze, R., and Coauthors, 2017: Large-eddy simulations over Germany using ICON: A comprehensive evaluation. *Quart. J. Roy. Meteor. Soc.*, **143**, 69–100, https://doi.org/10.1002/qj.2947.

Heymsfield, A. J., and Coauthors, 2008: Testing IWC retrieval methods using radar and ancillary measurements with in situ data. *J. Appl. Meteor. Climatol.*, **47**, 135–163, https://doi.org/10.1175/2007JAMC1606.1.

Hobbs, P. V., and A. J. Alkezweeny, 1968: The fragmentation of freezing water droplets in free fall. *J. Atmos. Sci.*, **25**, 881–888, https://doi.org/10.1175/1520-0469(1968)025<0881:TFOFWD>2.0.CO;2.

Hogan, R. J., and A. Bozzo, 2018: A flexible and efficient radiation scheme for the ECMWF model. *J. Adv. Model. Earth Syst.*, **10**, 1990–2008, https://doi.org/10.1029/2018MS001364.

Jackson, R. C., and G. M. McFarquhar, 2014: An assessment of the impact of antishattering tips and artifact removal techniques on bulk cloud ice microphysical and optical properties measured by the 2D cloud probe. *J. Atmos. Oceanic Technol.*, **31**, 2131–2144, https://doi.org/10.1175/JTECH-D-14-00018.1.

——, ——, J. Stith, M. Beals, R. A. Shaw, J. Jensen, J. Fugal, and A. Korolev, 2014: An assessment of the impact of antishattering tips and artifact removal techniques on cloud ice size distributions measured by the 2D cloud probe. *J. Atmos. Oceanic Technol.*, **31**, 2567–2590, https://doi.org/10.1175/JTECH-D-13-00239.1.

Karalis, M., G. Sotiropoulou, S. J. Abel, E. Bossioli, P. Georgakaki, G. Methymaki, A. Nenes, and M. Tombrou, 2022: Effects of secondary ice processes on a stratocumulus to cumulus transition during a cold-air outbreak. *Atmos. Res.*, **277**, 106302, https://doi.org/10.1016/j.atmosres.2022.106302.

Klein, S. A., and Coauthors, 2009: Intercomparison of model simulations of mixed-phase clouds observed during the ARM Mixed-Phase Arctic Cloud Experiment. I: Single-layer cloud. *Quart. J. Roy. Meteor. Soc.*, **135**, 979–1002, https://doi.org/10.1002/qj.416.

Klemp, J. B., J. Dudhia, and A. D. Hassiotis, 2008: An upper gravity-wave absorbing layer for NWP applications. *Mon. Wea. Rev.*, **136**, 3987–4004, https://doi.org/10.1175/2008MWR2596.1.

Korolev, A., and T. Leisner, 2020: Review of experimental studies of secondary ice production. *Atmos. Chem. Phys.*, **20**, 11 767–11 797, https://doi.org/10.5194/acp-20-11767-2020.

——, and Coauthors, 2017: Mixed-phase clouds: Progress and challenges. *Ice Formation and Evolution in Clouds and Precipitation: Measurement and Modeling Challenges*, *Meteor. Monogr.*, No. 58, Amer. Meteor. Soc., https://doi.org/10.1175/AMSMONOGRAPHS-D-17-0001.1.

Korolev, A. V., E. F. Emery, J. W. Strapp, S. G. Cober, G. A. Isaac, M. Wasey, and D. Marcotte, 2011: Small ice particles in tropospheric clouds: Fact or artifact? Airborne icing instrumentation evaluation experiment. *Bull. Amer. Meteor. Soc.*, **92**, 967–973, https://doi.org/10.1175/2010BAMS3141.1.

Lasher-Trapp, S., E. L. Scott, E. Järvinen, M. Schnaiter, F. Waitz, P. J. DeMott, C. S. McCluskey, and T. C. J. Hill, 2021: Observations and modeling of rime splintering in Southern Ocean cumuli. *J. Geophys. Res. Atmos.*, **126**, e2021JD035479, https://doi.org/10.1029/2021JD035479.

Lauber, A., A. Kiselev, T. Pander, P. Handmann, and T. Leisner, 2018: Secondary ice formation during freezing of levitated droplets. *J. Atmos. Sci.*, **75**, 2815–2826, https://doi.org/10.1175/JAS-D-18-0052.1.

Liu, Y., J. R. Key, S. A. Ackerman, G. G. Mace, and Q. Zhang, 2012: Arctic cloud macrophysical characteristics from CloudSat and CALIPSO. *Remote Sens. Environ.*, **124**, 159–173, https://doi.org/10.1016/j.rse.2012.05.006.

Luke, E. P., F. Yang, P. Kollias, A. M. Vogelmann, and M. Maahn, 2021: New insights into ice multiplication using remote-sensing observations of slightly supercooled mixed-phase clouds in the Arctic. *Proc. Natl. Acad. Sci. USA*, **118**, e2021387118, https://doi.org/10.1073/pnas.2021387118.

Maherndl, N., M. Maahn, M. Moser, J. Lucke, M. Mech, and N. Risse, 2023: Airborne observations of riming in Arctic mixed-phase clouds during HALO-(AC)3. *2023 EGU General Assembly*, Vienna, Austria, Amer. Geophys. Union, Abstract EGU23-5000, https://doi.org/10.5194/egusphere-egu23-5000.

McFarquhar, G. M., G. Zhang, M. R. Poellot, G. L. Kok, R. McCoy, T. Tooman, A. Fridlind, and A. J. Heymsfield, 2007: Ice properties of single-layer stratocumulus during the Mixed-Phase Arctic Cloud Experiment: 1. Observations. *J. Geophys. Res.*, **112**, D24201, https://doi.org/10.1029/2007JD008633.

Morrison, H., G. de Boer, G. Feingold, J. Harrington, M. D. Shupe, and K. Sulia, 2012: Resilience of persistent Arctic mixed-phase clouds. *Nat. Geosci.*, **5**, 11–17, https://doi.org/10.1038/ngeo1332.

Mossop, S. C., and J. Hallett, 1974: Ice crystal concentration in cumulus clouds: Influence of the drop spectrum. *Science*, **186**, 632–634, https://doi.org/10.1126/science.186.4164.632.

Murray, B. J., D. O'Sullivan, J. D. Atkinson, and M. E. Webb, 2012: Ice nucleation by particles immersed in supercooled cloud droplets. *Chem. Soc. Rev.*, **41**, 6519–6554, https://doi.org/10.1039/c2cs35200a.

Ono, A., 1969: The shape and riming properties of ice crystals in natural clouds. *J. Atmos. Sci.*, **26**, 138–147, https://doi.org/10.1175/1520-0469(1969)026<0138:TSARPO>2.0.CO;2.

Ovchinnikov, M., and Coauthors, 2014: Intercomparison of large-eddy simulations of Arctic mixed-phase clouds: Importance of ice size distribution assumptions. *J. Adv. Model. Earth Syst.*, **6**, 223–248, https://doi.org/10.1002/2013MS000282.

Pasquier, J. T., and Coauthors, 2022: Conditions favorable for secondary ice production in Arctic mixed-phase clouds. *Atmos. Chem. Phys.*, **22**, 15 579–15 601, https://doi.org/10.5194/acp-22-15579-2022.

Phillips, V. T. J., J.-I. Yano, and A. Khain, 2017: Ice multiplication by breakup in ice–ice collisions. Part I: Theoretical formulation. *J. Atmos. Sci.*, **74**, 1705–1719, https://doi.org/10.1175/JAS-D-16-0224.1.

——, S. Patade, J. Gutierrez, and A. Bansemer, 2018: Secondary ice production by fragmentation of freezing drops: Formulation and theory. *J. Atmos. Sci.*, **75**, 3031–3070, https://doi.org/10.1175/JAS-D-17-0190.1.

Possner, A., A. M. L. Ekman, and U. Lohmann, 2017: Cloud response and feedback processes in stratiform mixed-phase clouds perturbed by ship exhaust. *Geophys. Res. Lett.*, **44**, 1964–1972, https://doi.org/10.1002/2016GL071358.

Prenni, A. J., and Coauthors, 2007: Can ice-nucleating aerosols affect Arctic seasonal climate? *Bull. Amer. Meteor. Soc.*, **88**, 541–550, https://doi.org/10.1175/BAMS-88-4-541.

Rangno, A. L., and P. V. Hobbs, 2001: Ice particles in stratiform clouds in the Arctic and possible mechanisms for the production of high ice concentrations. *J. Geophys. Res.*, **106**, 15 065–15 075, https://doi.org/10.1029/2000JD900286.

Schemann, V., and K. Ebell, 2020: Simulation of mixed-phase clouds with the ICON large-eddy model in the complex Arctic environment around Ny-Ålesund. *Atmos. Chem. Phys.*, **20**, 475–485, https://doi.org/10.5194/acp-20-475-2020.

Schwarzenboeck, A., V. Shcherbakov, R. Lefevre, J.-F. Gayet, Y. Pointin, and C. Duroure, 2009: Indications for stellar-crystal fragmentation in Arctic clouds. *Atmos. Res.*, **92**, 220–228, https://doi.org/10.1016/j.atmosres.2008.10.002.

Seifert, A., and K. D. Beheng, 2006: A two-moment cloud microphysics parameterization for mixed-phase clouds. Part 1: Model description. *Meteor. Atmos. Phys.*, **92**, 45–66, https://doi.org/10.1007/s00703-005-0112-4.

Shupe, M. D., S. Y. Matrosov, and T. Uttal, 2006: Arctic mixed-phase cloud properties derived from surface-based sensors at SHEBA. *J. Atmos. Sci.*, **63**, 697–711, https://doi.org/10.1175/JAS3659.1.

Solomon, A., G. Feingold, and M. D. Shupe, 2015: The role of ice nuclei recycling in the maintenance of cloud ice in Arctic mixed-phase stratocumulus. *Atmos. Chem. Phys.*, **15**, 10 631–10 643, https://doi.org/10.5194/acp-15-10631-2015.

Sotiropoulou, G., S. Sullivan, J. Savre, G. Lloyd, T. Lachlan-Cope, A. M. L. Ekman, and A. Nenes, 2020: The impact of secondary ice production on Arctic stratocumulus. *Atmos. Chem. Phys.*, **20**, 1301–1316, https://doi.org/10.5194/acp-20-1301-2020.

——, L. Ickes, A. Nenes, and A. M. L. Ekman, 2021a: Ice multiplication from ice–ice collisions in the high Arctic: Sensitivity to ice habit, rimed fraction, ice type and uncertainties in the numerical description of the process. *Atmos. Chem. Phys.*, **21**, 9741–9760, https://doi.org/10.5194/acp-21-9741-2021.

——, E. Vignon, G. Young, H. Morrison, S. J. O'Shea, T. Lachlan-Cope, A. Berne, and A. Nenes, 2021b: Secondary ice production in summer clouds over the Antarctic coast: An underappreciated process in atmospheric models. *Atmos. Chem. Phys.*, **21**, 755–771, https://doi.org/10.5194/acp-21-755-2021.

Sulia, K. J., H. Morrison, and J. Y. Harrington, 2014: Dynamical and microphysical evolution during mixed-phase cloud glaciation simulated using the bulk adaptive habit prediction model. *J. Atmos. Sci.*, **71**, 4158–4180, https://doi.org/10.1175/JAS-D-14-0070.1.

Sullivan, S. C., C. Hoose, A. Kiselev, T. Leisner, and A. Nenes, 2018: Initiation of secondary ice production in clouds. *Atmos. Chem. Phys.*, **18**, 1593–1610, https://doi.org/10.5194/acp-18-1593-2018.

Tornow, F., A. S. Ackerman, and A. M. Fridlind, 2021: Preconditioning of overcast-to-broken cloud transitions by riming in marine cold air outbreaks. *Atmos. Chem. Phys.*, **21**, 12 049–12 067, https://doi.org/10.5194/acp-21-12049-2021.

Turner, D. D., S. A. Clough, J. C. Liljegren, E. E. Clothiaux, K. E. Cady-Pereira, and K. L. Gaustad, 2007: Retrieving liquid water path and precipitable water vapor from Atmospheric Radiation Measurement (ARM) microwave radiometers. *IEEE Trans. Geosci. Remote Sens.*, **45**, 3680–3690, https://doi.org/10.1109/TGRS.2007.903703.

van Diedenhoven, B., A. M. Fridlind, A. S. Ackerman, E. W. Eloranta, and G. M. McFarquhar, 2009: An evaluation of ice formation in large-eddy simulations of supercooled Arctic stratocumulus using ground-based lidar and cloud radar. *J. Geophys. Res.*, **114**, D10203, https://doi.org/10.1029/2008JD011198.

Vergara-Temprado, J., and Coauthors, 2018: Strong control of Southern Ocean cloud reflectivity by ice-nucleating particles. *Proc. Natl. Acad. Sci. USA*, **115**, 2687–2692, https://doi.org/10.1073/pnas.1721627115.

Verlinde, J., and Coauthors, 2007: The Mixed-Phase Arctic Cloud Experiment. *Bull. Amer. Meteor. Soc.*, **88**, 205–222, https://doi.org/10.1175/BAMS-88-2-205.

Waitz, F., M. Schnaiter, T. Leisner, and E. Järvinen, 2022: In situ observation of riming in mixed-phase clouds using the PHIPS probe. *Atmos. Chem. Phys.*, **22**, 7087–7103, https://doi.org/10.5194/acp-22-7087-2022.

Wang, Z., 2007: A refined two-channel microwave radiometer liquid water path retrieval for cold regions by using multiple-sensor measurements. *IEEE Geosci. Remote Sens. Lett.*, **4**, 591–595, https://doi.org/10.1109/LGRS.2007.900752.

Wegener, A., 1911: *Thermodynamik der Atmosphäre*. J. A. Barth, 331 pp.

Zängl, G., D. Reinert, P. Rípodas, and M. Baldauf, 2015: The ICON (ICOsahedral non-hydrostatic) modelling framework of DWD and MPI-M: Description of the non-hydrostatic dynamical core. *Quart. J. Roy. Meteor. Soc.*, **141**, 563–579, https://doi.org/10.1002/qj.2378.

Zhang, W., X. Shi, and C. Lu, 2022: Impacts of the ice-particle size distribution shape parameter on climate simulations with the Community Atmosphere Model version 6 (CAM6). *Geosci. Model Dev.*, **15**, 7751–7766, https://doi.org/10.5194/gmd-15-7751-2022.

Zhao, C., and Coauthors, 2012: Toward understanding of differences in current cloud retrievals of ARM ground-based measurements. *J. Geophys. Res.*, **117**, D10206, https://doi.org/10.1029/2011JD016792.

Zhao, M., L. Cao, L. Duan, G. Bala, and K. Caldeira, 2021: Climate more responsive to marine cloud brightening than ocean albedo modification: A model study. *J. Geophys. Res. Atmos.*, **126**, e2020JD033256, https://doi.org/10.1029/2020JD033256.

Zhao, X., X. Liu, V. T. J. Phillips, and S. Patade, 2021: Impacts of secondary ice production on Arctic mixed-phase clouds based on ARM observations and CAM6 single-column model simulations. *Atmos. Chem. Phys.*, **21**, 5685–5703, https://doi.org/10.5194/acp-21-5685-2021.